J. Fluid Mech. (2025), *vol.* 1014, A28, doi:10.1017/jfm.2025.10267

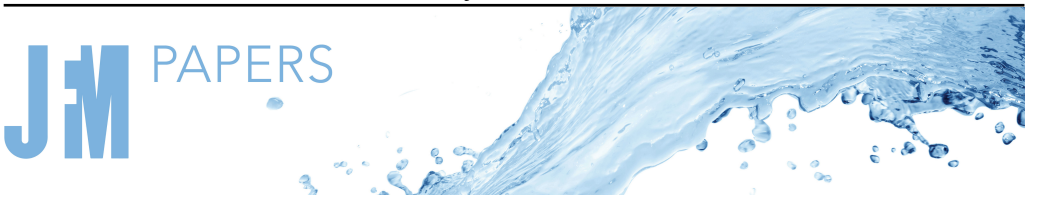

Two- and three-dimensional wake transitions of a circular cylinder with a rear-attached splitter plate

Hongyi Jiang

Ocean College, Zhejiang University, Zhoushan 316021, PR China

Corresponding author: Hongyi Jiang, hongyi.jiang@zju.edu.cn

(Received 13 May 2024; revised 31 March 2025; accepted 14 May 2025)

This study investigates the strong influence of a splitter plate on two- and three-dimensional wake transitions of a circular cylinder. Direct numerical simulations and Floquet analyses are conducted over a parameter space including Reynolds numbers (Re) of 10–480 and non-dimensional plate lengths (L/D) of 0–6. With the increase in L/D, the critical Re for the onset of vortex shedding (Re_{cr2D}) increases monotonically. The delayed onset of vortex shedding with elongation of the body is physically explained. The critical Re for the onset of three-dimensionality (Re_{cr3D}) and the three-dimensional wake instability modes and structures are also significantly altered by the splitter plate. Compared with an isolated cylinder, the Re_{cr3D} for $L/D = 1$ is significantly reduced via a long wavelength mode, whereas the Re_{cr3D} for $L/D = 2$–6 is significantly increased via other modes. For each L/D, with increasing Re over the wake transition process, the spanwise wavelength of the wake structure gradually decreases, and the wake structure becomes increasingly chaotic. The strong influence of the splitter plate on the formation of the primary vortices and three-dimensional wake structures alter the hydrodynamic characteristics strongly. In particular, optimal lift reduction is achieved at $L/D \sim 1$. In addition, the existence/absence of a hysteresis effect at the onset of three-dimensionality is identified by three methods. Among which, the method involving the Landau equation may be contaminated by initial transients induced by stable Floquet modes and may thus lead to a false conclusion on the existence/absence of hysteresis.

Key words: vortex instability, vortex shedding, wakes

1. Introduction

Steady incoming flow past a smooth circular cylinder has been a classical problem in fluid mechanics owing to its fundamental significance and extensive practical applications (Zdravkovich 1997). Although this canonical scenario is governed by a single dimensionless parameter, i.e. the Reynolds number Re ($= UD/\nu$, where U is the velocity of the incoming flow, D is the diameter of the cylinder and ν is the kinematic viscosity of the fluid), several flow transitions and flow regimes have been observed (e.g. Williamson 1996; Zdravkovich 1997). These include

(i) onset of two-dimensional (2-D) vortex shedding at $Re \sim 47$, where the wake starts to display the classical primary (Kármán) vortex street;
(ii) onset of three-dimensionality at $Re \sim 190$, where a relatively large-scale three-dimensional (3-D) wake structure (called mode A, with a spanwise period of $\sim 4D$) develops between adjacent primary vortices;
(iii) a gradual transition from mode A to a finer-scale 3-D structure (called mode B, with a spanwise period less than $1D$) over $Re \sim 230$–260;
(iv) successive transitions to turbulence in the wake, the separating shear layer and the boundary layer at $Re \sim 270$, 1200 and 2×10^5, respectively.

The flow regimes/transitions and the associated flow characteristics and hydrodynamic/aerodynamic behaviours of the body may be altered via various flow control techniques (Choi, Jeon & Kim 2008). Examples of passive control include attaching splitter plates to the cylinder (Roshko 1954, 1961; Apelt, West & Szewczyk 1973; Kwon & Choi 1996), adding small control cylinders (Strykowski & Sreenivasan 1990; Wang, Zhang & Wu 2006; Marquet, Sipp & Jacquin 2008) or other small bodies (Prasad & Williamson 1997) near the main cylinder, changing the surface roughness on the cylinder (Shih *et al.* 1993), etc. Examples of active control include applying various blowing/suction patterns on the cylinder surface (Dong, Triantafyllou & Karniadakis 2008; Poncet *et al.* 2008; Feng & Wang 2010), oscillating the cylinder in line with the incident flow (Xu, Zhou & Wang 2006), transverse to the incident flow (Williamson & Roshko 1988; Carberry, Sheridan & Rockwell 2005) or about its axis (Tokumaru & Dimotakis 1991), among many others. Although the flow control techniques may differ between one another, common purposes include (i) suppression of vortex shedding, (ii) suppression/mitigation of the fluctuating lift force and the associated vortex-induced vibration (VIV) (e.g. Cui, Feng & Hu 2022; Sun *et al.* 2022) and acoustic noise (e.g. You *et al.* 1998; Duan & Wang 2021) and (iii) drag force reduction.

One of the simplest yet effective flow control techniques in achieving the above-mentioned three purposes is to attach a splitter plate to the rear end of the cylinder. This arrangement delays the interaction between the two shear layers separated from the two sides of the cylinder and affects the vortex formation pattern (Roshko 1955). The basic scenario of a rear-attached splitter plate has also been extended upon by using e.g. a detached plate in the wake (Roshko 1954; Ozono 1999; Hwang, Yang & Sun 2003; Serson *et al.* 2014), dual rear-attached plates (Wang *et al.* 2019), a rear-attached wavy (Zhu & Liu 2020) or flexible plate (Duan & Wang 2021), a front-attached plate (Qiu *et al.* 2014; Chutkey, Suriyanarayanan & Venkatakrishnan 2018; Gao *et al.* 2019), both front- and rear-attached plates (Qiu *et al.* 2014; Gao *et al.* 2019) and by using a rear-attached splitter plate for bluff bodies other than a circular cylinder, e.g. a square cylinder (Ali, Doolan & Wheatley 2011; Chauhan *et al.* 2018), an elliptic cylinder (Soumya & Prakash 2017) or

Reference	L/D	Re	Mean drag	Vortex shedding from cylinder
Roshko (1954)	5	1.45×10^4	Marked reduction	Suppressed
Roshko (1961)	2.67	3.5×10^6–1×10^7	Small reduction	Suppressed
Gerrard (1966)	0–2	2×10^4		
Apelt *et al.* (1973)	0–2	1×10^4–5×10^4	Marked reduction	
Apelt & West (1975)	2–7	1×10^4–5×10^4	Marked reduction	Suppressed by $L/D > 5$
Kourta *et al.* (1987)	4.12	4.8×10^3	Marked reduction	Suppressed
Anderson & Szewczyk (1997)	0–1.75	3.5×10^4–4.6×10^4	Marked reduction	
Qiu *et al.* (2014)	3	6.9×10^4–3×10^5	Marked reduction	Suppressed
Gao *et al.* (2019)	0–2	3.33×10^4	Marked reduction	

Table 1. Experimental studies for flow past a circular cylinder with a rear-attached splitter plate.

a half-ellipse with a blunt trailing edge (Bearman 1965). Most of the above-mentioned scenarios produced various levels of reductions in the mean drag and/or fluctuating lift, as well as alterations in the vortex shedding frequency.

The present study focuses on the most canonical scenario of a circular cylinder with a rear-attached splitter plate. Early studies by Roshko (1954, 1961) examined both subcritical and transcritical Re values, and showed that a splitter plate was effective in reducing the mean drag and base pressure on the cylinder. For example, at a subcritical Re of 1.45×10^4, the use of a splitter plate with a non-dimensional length $L/D = 5$ resulted in a marked reduction in the mean drag coefficient from 1.15 to 0.72 (Roshko 1954,1961). Similar drag reduction behaviours were also observed by most of the experimental studies summarised in table 1. In addition, Gao *et al.* (2019) also reported a significant reduction in the fluctuating lift on the cylinder with L/D up to 2.

As for the influence on the vortex shedding, Apelt & West (1975) examined a range of $L/D = 2$–7 and found that, for $L/D > 5$, vortex shedding from the cylinder was suppressed by the plate, and instead vortex shedding developed from the trailing edge of the plate. This phenomenon was also reported by Roshko (1961), Kourta *et al.* (1987) and Qiu *et al.* (2014), where relatively long plates ($L/D \geq 2.67$) were tested. In contrast, Gerrard (1966), Apelt *et al.* (1973), Anderson & Szewczyk (1997) and Gao *et al.* (2019) examined cases with $L/D \leq 2$ and did not report suppression of vortex shedding from the cylinder. Instead, Gerrard (1966), Apelt *et al.* (1973) and Anderson & Szewczyk (1997) focused on the influence of L/D on the vortex shedding frequency, and found that the shedding frequency was altered in a non-monotonic fashion with the increase in L/D.

While the experimental studies summarised in table 1 generally focused on the range of $Re \gtrsim \mathrm{O}(10^4)$, previous numerical studies, summarised in table 2, focused on $Re \sim \mathrm{O}(10^2$–$10^3)$ instead. Specifically, Kwon & Choi (1996), Vu, Ahn & Hwang (2016) and de Araujo, Schettini & Silvestrini (2018) conducted 2-D numerical simulations and quantified the influence of Re and L/D on the vortex shedding frequency and the marked reductions in the mean drag and fluctuating lift coefficients. In addition, Serson *et al.* (2014) and de Araujo *et al.* (2018) extended the numerical simulations to a few 3-D cases, and examined the influence of Re and L/D on the vortex shedding frequency (but not on the drag or lift coefficient). Although the 3-D results were limited to only a few cases on the vortex shedding frequency, they suggested that the flow three-dimensionality played a significant role in altering the hydrodynamic characteristics.

Reference	Dimensions	L/D	Re	Mean drag	Fluctuating lift
Kwon and Choi (1996)	2-D	0–8	80–160	Marked reduction	
Vu *et al.* (2016)	2-D	0–6	60–240	Marked reduction	Marked reduction
de Araujo *et al.* (2018)	2-D	0–4.5	100, 160	Marked reduction	
Serson *et al.* (2014)	3-D	1	200, 300		
de Araujo *et al.* (2018)	3-D	0–2	300, 1250		

Table 2. Two- and three-dimensional numerical studies for flow past a circular cylinder with a rear-attached splitter plate.

In addition, the Floquet analyses of Serson *et al.* (2014) and Wang *et al.* (2019), for the cases of a detached splitter plate (with $L/D = 1$ and a gap between the cylinder and the plate being $G/D = 0.5$–3) and dual-attached splitter plates, respectively, showed that different types of placement of plates in the cylinder wake may significantly alter the critical Re for the 3-D wake transition and the 3-D wake instability modes.

However, for the more canonical scenario of an attached splitter plate, there has been no investigation in the literature on the onset of 3-D wake transition, (linear) 3-D wake instability modes, (nonlinear) 3-D wake structures and the significant influence of the three-dimensionality on the hydrodynamic characteristics (other than merely a few cases on the vortex shedding frequency).

To address these knowledge gaps, the present study carries out a systematic investigation on the influence of an attached splitter plate on the 2-D and 3-D wake transitions, 3-D wake instability modes, 3-D wake structures and the influence of the three-dimensionality on the hydrodynamic characteristics (e.g. the mean drag and fluctuating lift on the cylinder and the splitter plate). A relatively large parameter space of $Re = 10$–480 and $L/D = 0$–6 is examined, covering both the 2-D and 3-D wake transition regimes.

2. Numerical model

2.1. *Numerical method*

In the present study, the flow was solved by the direct numerical simulation (DNS) framework embedded in the open-source code Nektar++ (Cantwell *et al.* 2015). The governing equations for the flow were the continuity and incompressible Navier–Stokes equations

$$\nabla \cdot \boldsymbol{u} = 0, \tag{2.1}$$

$$\frac{\partial \boldsymbol{u}}{\partial t} + \boldsymbol{u} \cdot \nabla \boldsymbol{u} = -\nabla p + \nu \nabla^2 \boldsymbol{u}, \tag{2.2}$$

where $\boldsymbol{u}(\boldsymbol{x}, t) = (u_x, u_y, u_z)(x, y, z, t)$ is the velocity field, u_x, u_y and u_y denote the velocity components in the streamwise (x), transverse (y) and spanwise (z) directions, respectively, $p(\boldsymbol{x}, t)$ is the kinematic pressure (pressure divided by fluid density), t is time and ν is kinematic viscosity of the fluid. Equations (2.1) and (2.2) were solved by the unsteady Navier–Stokes solver embedded in Nektar++, together with the use of a velocity correction scheme (Karniadakis, Israeli & Orszag 1991), a second-order implicit–explicit time-integration scheme and a continuous Galerkin projection. A high-order spectral element method (Karniadakis & Sherwin 2005) was used for the x–y plane. For the 3-D DNS, a Fourier expansion was used in the geometrically homogeneous spanwise direction (Karniadakis 1990).

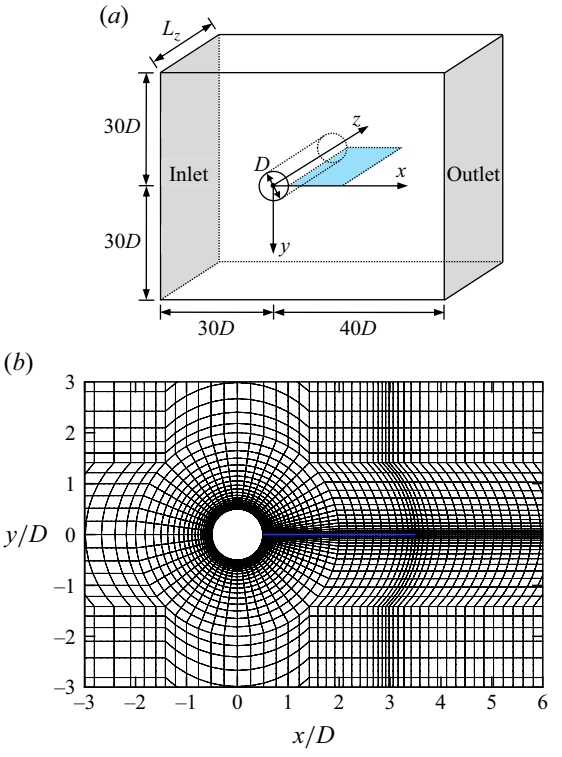

Figure 1. Computational domain and mesh for the case of flow past a circular cylinder with a splitter plate attached: (*a*) schematic model of the computational domain (not to scale), and (*b*) close-up view of the macro-element mesh near the cylinder–plate system for the case $L/D = 3$. The splitter plate is highlighted in blue.

2.2. *Computational domain and mesh*

A hexahedral computational domain, as sketched in figure 1(*a*), was used for the 3-D DNS, while the corresponding domain in the x–y plane was used for the 2-D DNS. A circular cylinder was placed at $(x, y) = (0, 0)$, while a splitter plate of zero thickness, as highlighted in blue, was attached to the rear end of the cylinder. The boundary conditions for the computational domain included a uniform velocity $(u_x, u_y, u_z) = (U, 0, 0)$ at the inlet and transverse sides, a zero normal velocity gradient at the outlet and a no-slip condition at the cylinder and plate surfaces. The boundary conditions for the pressure included a reference value of zero at the outlet, and a high-order Neumann condition (Karniadakis *et al.* 1991) at all other boundaries. For the 3-D DNS, periodic boundary conditions were employed at the two boundaries perpendicular to the cylinder span. The internal flow followed an impulsive start.

The computational mesh in the x–y plane consisted of approximately 10 000 macro-elements. Figure 1(*b*) shows a close-up view of the macro-element mesh near the cylinder–plate system for the case $L/D = 3$. Local mesh refinements were made around the cylinder and plate. The cylinder surface was discretised with 64 macro-elements, while the height of the first layer of elements next to the cylinder was $0.00553D$. At the trailing edge of the splitter plate, the element size was locally refined to $0.0667D \times 0.0320D$. To capture detailed wake evolution along the streamwise direction, a relatively high resolution was used in the wake region by specifying the streamwise size of the elements at the wake centreline ($y = 0$) increasing linearly from $0.167D$ at $x/D = (L/D + 1)$ to $0.5D$

Case description	St	$\overline{C_{D,cyl}}$	$C'_{L,cyl}$	$\overline{C_{D,plate}}$	$C'_{L,plate}$
$N_p = 3$	0.1230	0.8861	0.2002	−0.0523	1.2813
$N_p = 4$	0.1230	0.8859	0.1992	−0.0522	1.2783
$N_p = 5$ (Reference case)	0.1230	0.8859	0.1992	−0.0520	1.2782
$N_p = 6$	0.1230	0.8859	0.1992	−0.0519	1.2782

Table 3. Results of the 2-D mesh dependence study for the case $L/D = 4$ and $Re = 480$.

at $x/D = 30.5$. The macro-elements were then subdivided using high-order Lagrange polynomials on the Gauss–Lobatto–Legendre points for the quadrilateral expansions. Fifth-order polynomials ($N_p = 5$) were used for the 2-D DNS and Floquet analysis, while fourth-order polynomials ($N_p = 4$) were used for the 3-D DNS. The non-dimensional time-step size $\Delta tU/D$ was 0.0025 for $N_p = 5$ and 0.004 for $N_p = 4$, which corresponded to a Courant–Friedrichs–Lewy limit of no more than 0.6.

2.3. *Mesh convergence*

A mesh dependence study was performed based on the case $L/D = 4$ and $Re = 480$ (the largest Re considered in the present study). Firstly, 2-D DNSs were used to examine the adequacy of the mesh resolution in the x–y plane. In additional to the reference case with $N_p = 5$, three variation cases with $N_p = 3$, 4 and 6 were computed. Table 3 lists the numerical results predicted by different mesh resolutions. The Strouhal number (St) for the cylinder–plate system and the drag and lift coefficients (C_D and C_L) on the cylinder/plate are calculated as

$$St = \frac{f_L D}{U}, \tag{2.3}$$

$$C_D = \frac{F_D}{\frac{1}{2}\rho U^2 D}, \tag{2.4}$$

$$C_L = \frac{F_L}{\frac{1}{2}\rho U^2 D}, \tag{2.5}$$

where f_L is the peak frequency obtained from the fast Fourier transform of the time history of C_L, while F_D and F_L are the drag and lift forces on the cylinder/plate (per unit span length). The time-averaged drag and lift coefficients are denoted $\overline{C_D}$ and $\overline{C_L}$, respectively. The root-mean-square lift coefficient (C'_L) is calculated as

$$C'_L = \sqrt{\frac{1}{N}\sum_{i=1}^{N}\left(C_{L,i} - \overline{C_L}\right)^2}, \tag{2.6}$$

where N is the data length in the time history of C_L. The forces on the cylinder and plate are distinguished by the subscripts 'cyl' and 'plate', respectively. As shown in table 3, the hydrodynamic forces predicted with $N_p \geq 4$ are practically unchanged, which suggested that the mesh resolution in the x–y plane was adequate.

The 3-D mesh dependence study focused on the adequacy of the spanwise domain length ($L_z/D = 16$) and spanwise resolution (128 Fourier planes) used for the reference case. Two variation cases were considered.

Case description	St	$\overline{C_{D,cyl}}$	$C'_{L,cyl}$	$\overline{C_{D,plate}}$	$C'_{L,plate}$
Reference case	0.126	0.876	0.169	−0.0654	1.066
Increase in spanwise domain length	0.126	0.876	0.166	−0.0650	1.045
Increase in spanwise resolution	0.126	0.876	0.165	−0.0655	1.041

Table 4. Results of the 3-D mesh dependence study for the case $L/D = 4$ and $Re = 480$.

Case description	St	$\overline{C_{D,cyl}}$	$C'_{L,cyl}$	$\overline{C_{D,plate}}$	$C'_{L,plate}$
$L_z/D = 16$	0.156	1.073	0.108	−0.0156	0.0936
$L_z/D = 32$ (Reference case)	0.154	1.073	0.0646	−0.0156	0.0558
$L_z/D = 64$	0.154	1.073	0.0526	−0.0156	0.0454

Table 5. Results of the L_z dependence study for the case $L/D = 1$ and $Re = 180$.

(i) Variation case 1: the spanwise domain length was increased by 1.5 times to $L_z/D = 24$, while the spanwise resolution was unchanged (i.e. 192 Fourier planes for $L_z/D = 24$); and.
(ii) variation case 2: the spanwise resolution was increased by 1.5 times through using 192 Fourier planes over $L_z/D = 16$.

For each 3-D case, at least 400 non-dimensional time units (defined as $t^* = tU/D$) were used to wash out the initial transients. After that, at least another 500 time units were used for the statistics. Table 4 lists the hydrodynamic coefficients calculated with the three cases. The close agreement in the coefficients suggested that the spanwise domain length and resolution used by the reference case were adequate.

For $L/D \leq 0.5$ and $L/D \geq 4$, the most unstable spanwise wavelengths of the 3-D wake instability modes predicted by the Floquet analysis (to be presented in § 4) were no more than $4.11D$, such that the use of $L_z/D = 16$ for the 3-D DNS accommodated at least three spanwise periods of the unstable mode, which was deemed adequate (Jiang, Cheng & An 2017). For $L/D = 1$–3, however, the most unstable wavelengths for the 3-D wake instability modes were more than $10D$, such that an increased L_z/D of 32 was used (together with the use of 256 Fourier planes so as to keep the spanwise resolution unchanged). The adequacy of $L_z/D = 32$ was examined based on the case $L/D = 1$ and $Re = 180$ (the smallest Re for the 3-D DNS of $L/D = 1$, where the unstable wavelength was the largest). Table 5 lists the hydrodynamic coefficients obtained with $L_z/D = 16$, 32 and 64, which suggested that the use of $L_z/D = 32$ was adequate.

3. Onset of vortex shedding

For an isolated circular cylinder, the 2-D vortex shedding emerges as a result of a Hopf bifurcation at a critical Re (Re_{cr2D}) of approximately 47 (e.g. Henderson 1997). Similarly, figure 2 quantifies the Re_{cr2D} values for a circular cylinder with a no-slip splitter plate of $L/D = 0$–6. The Re_{cr2D} for each L/D is determined by the method introduced in Appendix A. As shown in figure 2, with the increase in L/D, the Re_{cr2D} value increases monotonically (but not linearly). Since the Re_{cr2D}–L/D relationship is not reported in

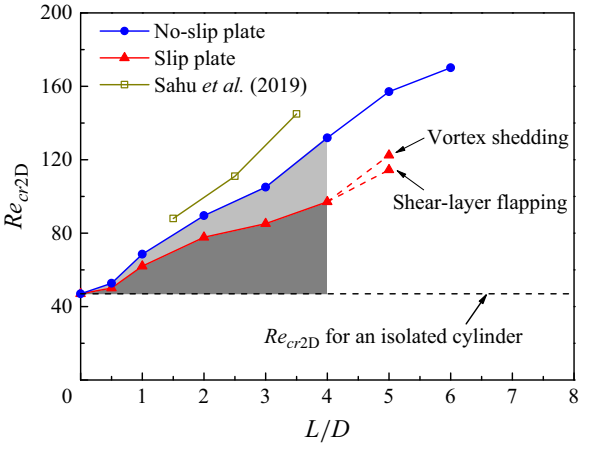

Figure 2. Critical Re for the onset of vortex shedding for a circular cylinder with a rear-attached splitter plate of either no-slip or slip boundary condition.

the literature, the present Re_{cr2D}–L/D relationship is compared with the Re_{cr2D}–L/D relationship for a slightly different scenario by Sahu, Furquan & Mittal (2019), whose rear-attached splitter plate had a finite thickness of $0.2D$ (in contrast to a zero thickness plate for the present study). Although the results do not match quantitatively due to the use of different plate thicknesses, the Re_{cr2D}–L/D relationship by Sahu *et al.* (2019) also showed a monotonic but nonlinear increase in Re_{cr2D}, which is qualitatively similar to the variation trend of the present Re_{cr2D}–L/D relationship.

For the present scenario with different L/D values, figure 3(*a–d*) illustrates instantaneous spanwise vorticity (ω_z) fields at Re slightly above Re_{cr2D}, where ω_z is defined in a non-dimensional form as

$$\omega_z = \left(\frac{\partial u_y}{\partial x} - \frac{\partial u_x}{\partial y}\right)\frac{D}{U}. \tag{3.1}$$

With the increase in L/D, the streamwise location of vortex shedding is pushed further downstream. Physically, the splitter plate is a boundary with a no-penetration condition ($u_y = 0$) and a no-slip condition ($u_x = 0$). The two conditions induce an increase in Re_{cr2D} with increase in L/D through two effects.

(i) Effect of the no-penetration condition. The shear layers separated from the two sides of the cylinder are gradually weakened with distance downstream (e.g. the vorticity in the shear layer gradually reduces with distance downstream). When the instability of the separating shear layers and the formation and shedding of the vortices are restricted by the no-penetration condition of the plate and are forced to develop further downstream with increasing L/D, the separating shear layers at the location of vortex shedding are further weakened. Therefore, an increased Re_{cr2D} is required for the shear layers to gain more strength to roll up into vortices.

(ii) Effect of the no-slip condition. The shear layers developed on the two sides of the no-slip plate are of opposite sign of vorticity to the shear layers separated from the cylinder (figure 3*a–d*) and further weaken the latter, which induces a further increased Re_{cr2D} for the generation of vortices.

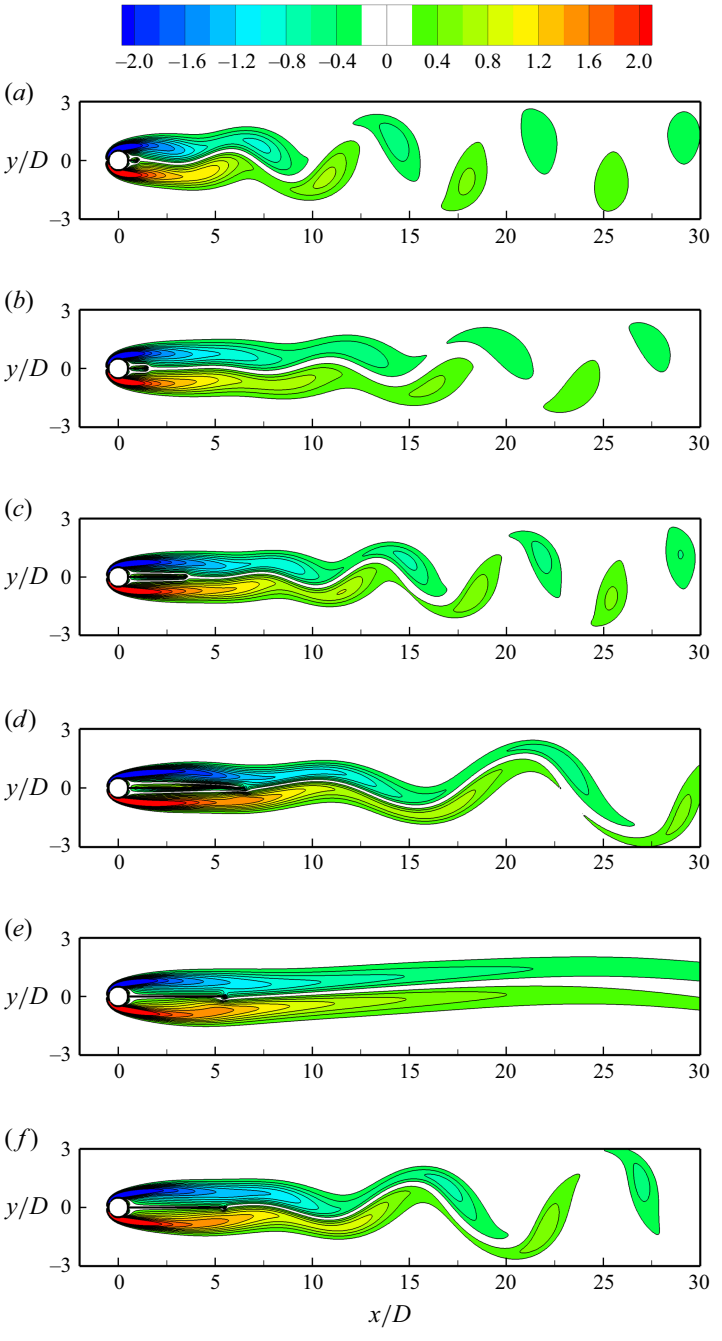

Figure 3. Instantaneous spanwise vorticity fields at Re slightly above Re_{cr2D}: (*a*) (L/D, Re) = (0.5, 60), (*b*) (L/D, Re) = (1, 70), (*c*) (L/D, Re) = (3, 110), (*d*) (L/D, Re) = (6, 180), (*e*) (L/D, Re) = (5, 120) with a slip splitter plate and (*f*) (L/D, Re) = (5, 130) with a slip splitter plate.

To quantitatively reveal individual contribution of the no-penetration condition and no-slip condition, we introduce a specifically designed case with a splitter plate using a slip boundary condition ($\partial u_x/\partial y = 0$, $u_y = 0$ and a high-order Neumann condition for

the pressure). By replacing the no-slip plate with the slip plate, the no-slip condition is removed whereas the no-penetration condition is preserved. The Re_{cr2D} values for the cases with no-slip and slip plates are both shown in figure 2. For the slip plate cases, the focus is placed on $L/D \leq 4$, because for $L/D = 5$ an additional flow regime is observed in between of the steady regime ($Re \lesssim 110$) and the vortex shedding regime ($Re \gtrsim 125$; figure 3*f*), over which the separating shear layers display a low-frequency (∼1/6 times the vortex shedding frequency) periodic flapping behaviour, without generation of vortices (figure 3*e*). As shown in figure 2, the cases with the slip plate (the red curve) divide the increase in Re_{cr2D} (the shaded area) into two parts. The darker area represents the increase in Re_{cr2D} induced by the no-penetration condition, while the lighter area represents the further increase in Re_{cr2D} induced by the no-slip condition. The contribution by the no-penetration condition is more significant (which accounts for ∼60 %–70 % of the increase in Re_{cr2D}), while the no-slip condition also plays an important role.

It is worth noting that, in the present context, the onset/suppression of vortex shedding quantified in figure 2 is with respect to the entire cylinder–plate system, which is different from the 'suppression' of vortex shedding from the cylinder and a transfer of vortex shedding to the trailing edge of the plate reported by Roshko (1961), Apelt & West (1975), Kourta *et al.* (1987) and Qiu *et al.* (2014) with $Re \gtrsim \mathrm{O}(10^4)$ and relatively long plate lengths ($L/D \geq 2.67$). When the vortex shedding is directed away from the cylinder by the plate, the effect of vortex shedding on the cylinder is weakened but not fully eliminated. This feature is reflected by a reduction (but not suppression) in the fluctuating lift on the cylinder shown later on in figure 17(*b*). The 'suppression' of vortex shedding from the cylinder reported by the experimental studies of Roshko (1961), Apelt & West (1975), Kourta *et al.* (1987) and Qiu *et al.* (2014) may be better interpreted as a mitigation of the effect of vortex shedding on the cylinder.

4. Three-dimensional wake transition

Beyond a specific critical Re for the onset of three-dimensionality (denoted Re_{cr3D}), 3-D flow structures develop in the wake and may alter the hydrodynamic forces on the cylinder and the plate. In this section, the 3-D wake transitions for $L/D = 0$–6 are examined through both Floquet stability analysis and 3-D DNS. The Floquet analysis, which follows that reported by Barkley & Henderson (1996), is used to determine the Re_{cr3D} value for the onset of three-dimensionality and to identify the 3-D wake instability modes. Figure 4 summarises the critical Re and spanwise wavelength (λ) for the 3-D wake instability modes determined by the Floquet analysis. With the increase in L/D, the first 3-D wake instability mode observed at Re_{cr3D} changes in the sequence of (i) mode A for $L/D = 0$–0.5, (ii) mode AL for $L/D = 1$, (iii) mode BL for $L/D = 2$–3 and (iv) mode QP3 for $L/D = 4$–6. For modes AL and BL, the first letter represents a spatio-temporal symmetry pattern similar to that for mode A or B for an isolated cylinder, i.e.

Symmetry pattern of the mode A type

$$\omega_x\,(x,\,y,\,z,\,t) = -\omega_x\,(x,\,-y,\,z,\,t+T/2)\,. \tag{4.1}$$

Symmetry pattern of the mode B type

$$\omega_x\,(x,\,y,\,z,\,t) = \omega_x\,(x,\,-y,\,z,\,t+T/2)\,, \tag{4.2}$$

where ω_x is the streamwise vorticity defined in a non-dimensional form as

$$\omega_x = \left(\frac{\partial u_z}{\partial y} - \frac{\partial u_y}{\partial z}\right)\frac{D}{U}, \tag{4.3}$$

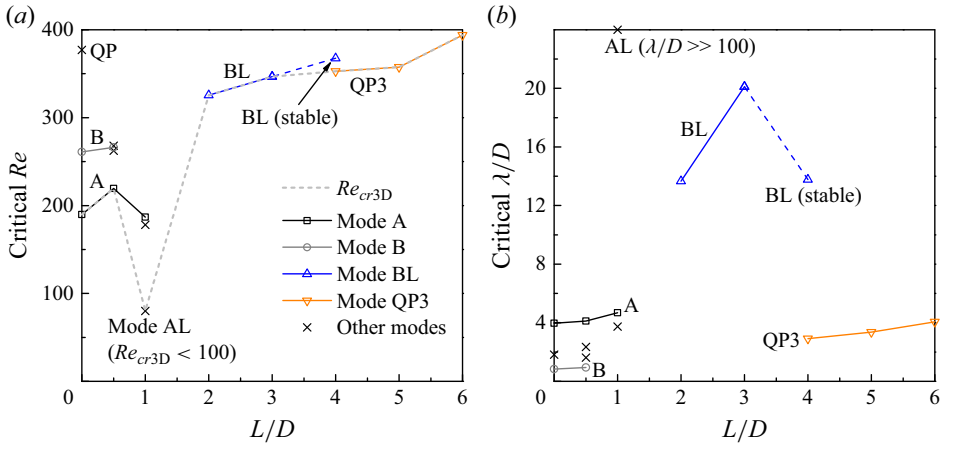

Figure 4. Floquet analysis results for various L/D conditions: (a) critical Re for the 3-D wake instability modes, and (b) critical λ/D for these modes.

and T is the vortex shedding period. The second letter, L, indicates a long spanwise wavelength (of more than ten times larger than that for the conventional mode A or B for an isolated cylinder, see figure 4b). In addition, three quasi-periodic (QP) modes are observed for the cases with a splitter plate, which are named QP1, QP2 (for $L/D = 0.5$) and QP3 (for $L/D = 4$–6). It is worth noting that the Re_{cr3D} values and 3-D wake instability modes summarised in figure 4 for the present scenario with an attached splitter plate are significantly different from those reported by Serson *et al.* (2014) and Wang *et al.* (2019) for the scenarios with other types of placement of plates in the cylinder wake (a detached splitter plate and dual-attached splitter plates, respectively), which demonstrates the necessity of the present investigation.

In addition to the Floquet analysis, 3-D DNSs are used to reveal the unstable modes and overall wake structures for the real 3-D flows, and to obtain statistically stationary hydrodynamic forces over the 3-D wake transition regimes. For each 3-D case, the statistical time period spans at least 400 non-dimensional time units, after discarding an initial transient period of at least another 400 time units.

Owing to the significant variations in the 3-D wake instability modes and the critical Re and λ/D values with L/D (figure 4), the Floquet analysis and 3-D DNS results for $L/D = 0$–0.5, 1, 2–3 and 4–6 are presented separately in §§ 4.1–4.4, respectively.

4.1. *Three-dimensional results for L/D = 0–0.5*

The 3-D results for $L/D = 0.5$ are relatively similar to those for an isolated cylinder, and are therefore reported first. Figure 5(a) shows the dependence of the dominant Floquet multiplier μ on the spanwise wavenumber β ($= 2\pi/\lambda$) for several Re values, where four wake instability modes are detected. Based on the $|\mu|$–β relationships predicted at a number of Re values, the neutral instability curves for the four modes are mapped out in figure 5(b).

Figure 6 shows the streamwise perturbation vorticity fields for the four modes. The perturbation patterns shown in figure 6(a,d), which display opposite signs and same sign for the two sides of the wake centreline, respectively, agree with the patterns of modes A and B for an isolated cylinder (see e.g. Carmo, Meneghini & Sherwin 2010). In addition, the critical spanwise wavelengths for modes A and B, which are determined at the left tip of the corresponding neutral curve (figure 5b) as $4.11D$ and $0.94D$, respectively, remain

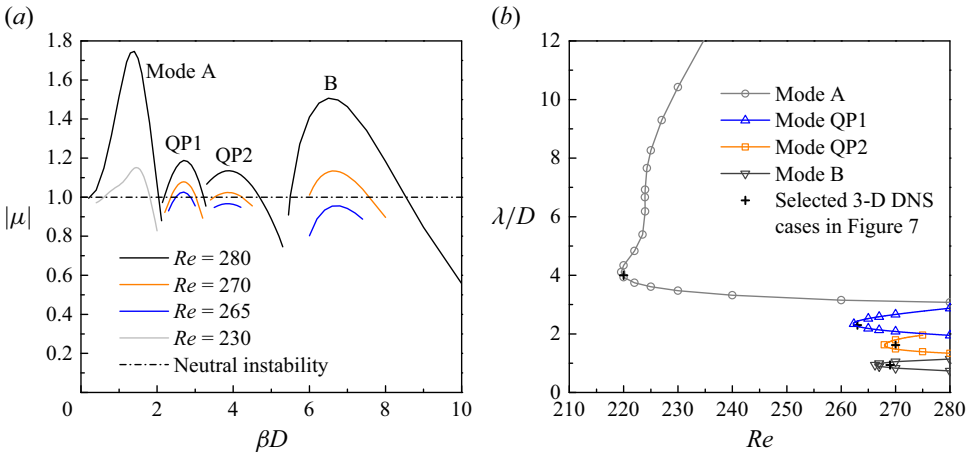

Figure 5. Floquet analysis results for $L/D = 0.5$: (*a*) the $|\mu|$–β relationships for several Re values, and (*b*) the neutral instability curves for the 3-D wake instability modes.

similar to those of modes A and B for an isolated cylinder (e.g. $3.97D$ and $0.83D$ by Posdziech & Grundmann (2001)). As for the critical Re values for modes A and B, the present results of 219.6 and 266.2 are slightly larger than those for an isolated cylinder (e.g. 190.2 and 261.0 by Posdziech & Grundmann (2001)), which suggests that a short splitter plate is able to delay the onset of three-dimensionality slightly.

In addition to the synchronous modes A and B, two QP modes are observed for $L/D = 0.5$ (figure 5). The streamwise perturbation vorticity fields for the two QP modes display irregular arrangement of both signs at each side of the wake centreline (figure 6*b*,*c*). The critical Re values for the two QP modes (262.3 and 267.9) are much smaller than that for the QP mode of an isolated cylinder (e.g. 377 by Blackburn, Marques & Lopez (2005)).

To further confirm the existence of the four unstable modes shown in figures 5 and 6, 3-D DNSs are used to reveal their 3-D structures. The 3-D DNSs are performed with Re and L_z ($= \lambda$) close to the left tip of each neutral instability curve (marked by + in figure 5*b*), such that the wake is only unstable to one mode, and the 3-D structure is relatively regular. Figure 7 shows the streamwise and spanwise vorticity structures corresponding to the four modes. The modes A and B structures shown in figure 7(*a*,*d*) display out-of-phase and in-phase sequences between the neighbouring streamwise vortices along the streamwise direction, respectively, which are consistent with those for the modes A and B structures for an isolated cylinder (see e.g. Williamson 1996). In contrast, the two QP structures display travelling waves moving in the spanwise direction, which are similar to the QP structure for an isolated cylinder reported by Blackburn *et al.* (2005). The travelling waves for the QP modes explain the irregular patterns of the streamwise perturbation vorticity fields shown in figure 6(*b*,*c*).

To allow for complex interactions among the wake instability modes, 3-D DNSs are also performed with a sufficiently long spanwise domain length of $L_z/D = 16$, which may accommodate four spanwise periods of the longest wavelength mode. As Re exceeds Re_{cr3D} of 219.6, the first flow regime observed at $Re = 220$ and 230 is represented by the development of four spanwise periods of ordered mode A structure (figure 8*a*), followed by the development of vortex dislocations and disordered mode A structure in the fully developed flow (figure 8*b*). With the increase in Re to 240 and 260, a mode swapping (over time) between the relatively large-scale mode A structure and the finer-scale structures

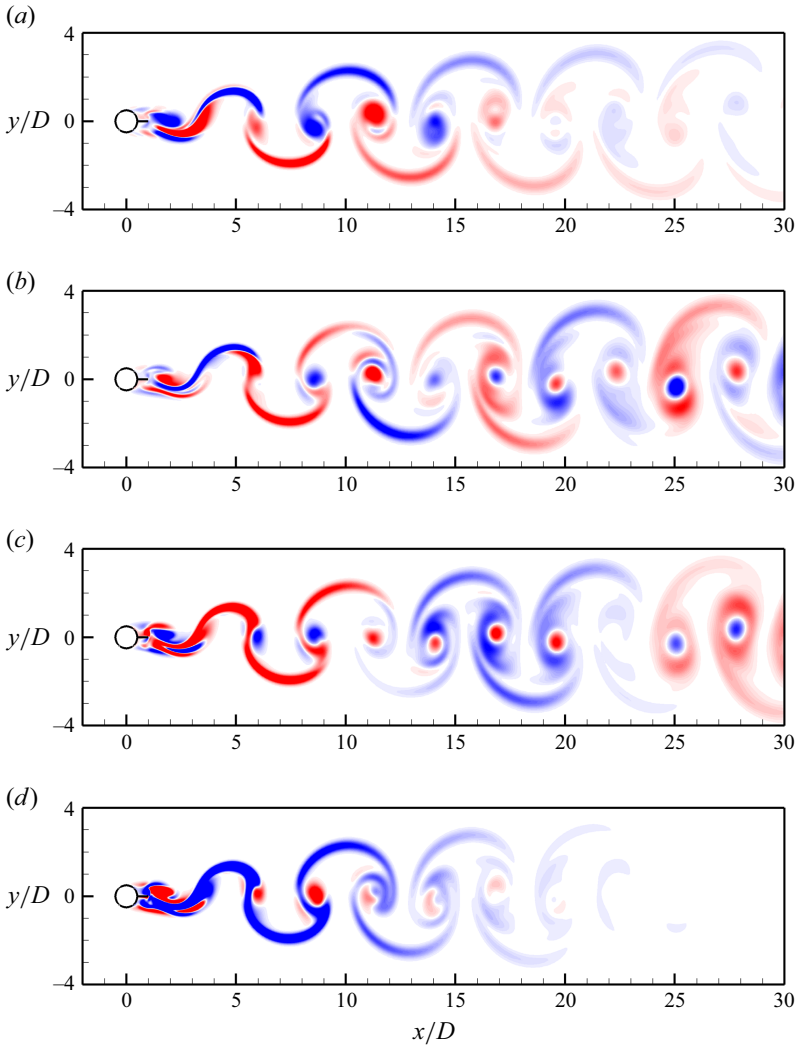

Figure 6. Streamwise perturbation vorticity fields for the case $(L/D, Re) = (0.5, 280)$: (*a*) mode A predicted at $\beta D = 1.4$, (*b*) mode QP1 predicted at $\beta D = 2.7$, (*c*) mode QP2 predicted at $\beta D = 3.9$ and (*d*) mode B predicted at $\beta D = 6.5$. Red and blue denote positive and negative vorticity values, respectively.

(figure 8*c*) is observed. Owing to the influence of the mode A streamwise vortices and their influence back onto the spanwise vortices (i.e. the base flow), the finer-scale structures appear in the real 3-D flow earlier than their critical *Re* values predicted by the Floquet analysis (at $Re \geq 262.3$). As *Re* increases from 240 to 260, the dominant wake pattern changes from the mode A structure to the finer-scale structures. A difference to the mode swapping between modes A and B for the case of an isolated cylinder (Williamson 1996) is that, for the case of $L/D = 0.5$, it is difficult to determine the types of modes for the finer-scale structures, since mode B and the two QP modes become unstable to the base flow at very similar *Re* values (figure 5*b*). Beyond the mode swapping regime, the present DNSs show that the wakes of $Re = 280$–400 are always represented by the small-scale structures (e.g. figure 8*d*). Regardless of the types of modes for the small-scale structures, over this flow regime the wake becomes increasingly chaotic and turbulent.

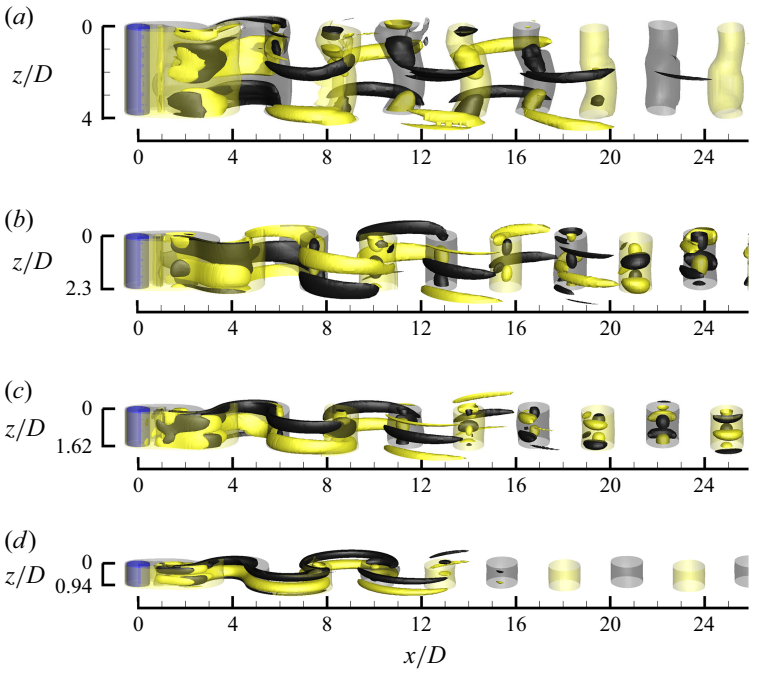

Figure 7. Instantaneous vorticity fields for the 3-D wake instability modes observed for $L/D = 0.5$: (*a*) mode A structure at $(Re, L_z/D) = (220, 4.0)$, (*b*) mode QP1 structure at $(Re, L_z/D) = (263, 2.3)$, (*c*) mode QP2 structure at $(Re, L_z/D) = (270, 1.62)$ and (*d*) mode B structure at $(Re, L_z/D) = (269, 0.94)$. The translucent iso-surfaces represent spanwise vortices with $|\omega_z| = 0.5$, while the opaque iso-surfaces represent streamwise vortices with $|\omega_x| = 0.5$, 0.1, 0.1 and 0.2 for panels (*a–d*), respectively. Dark grey and light yellow denote positive and negative vorticity values, respectively. The flow is from left to right past the cylinder on the left.

4.2. *Three-dimensional results for L/D = 1*

The 3-D results for $L/D = 1$ are completely different from those for $L/D = 0$ and 0.5. Figure 9(*a*) shows the first three unstable modes for $L/D = 1$ predicted by the Floquet analysis, while figure 10 shows the streamwise perturbation vorticity fields for the three modes. For $L/D = 1$, the first unstable mode is a long wavelength mode AL with a spatio-temporal symmetry pattern of the mode A type (figure 10*a*). Figure 9(*b*) shows the neutral instability curve for mode AL. Unlike conventional 3-D wake instability modes which are unstable over a finite range of spanwise wavelengths (cf. e.g. figure 5), mode AL is marginally unstable towards $\beta D \to 0$ (figure 9*a*), i.e. $\lambda/D \to \infty$ (figure 9*b*). The critical Re for the onset of mode AL is well below 100, while the unstable wavelength λ/D is of the order of 10^2. The emergence of the unconventional mode AL for $L/D = 1$ coincides with the strong influence of a splitter plate of $L/D = 1$ in altering the base flow by directing the vortex formation downstream of the plate.

In addition to mode AL, two additional synchronous modes are observed in figure 9(*a*), and their spatio-temporal symmetry patterns are of the mode A and B types, respectively (figure 10*b*,*c*). Nevertheless, the perturbation pattern shown in figure 10(*c*) is somewhat different from that of the conventional mode B shown in figure 6(*d*). Although the three synchronous modes observed in figure 9 may not represent a complete set of the unstable modes over the wake transition regimes, Floquet analyses are limited to $Re \leq 200$, because (i) above this the real 3-D flow is expected to be governed by complex interactions of

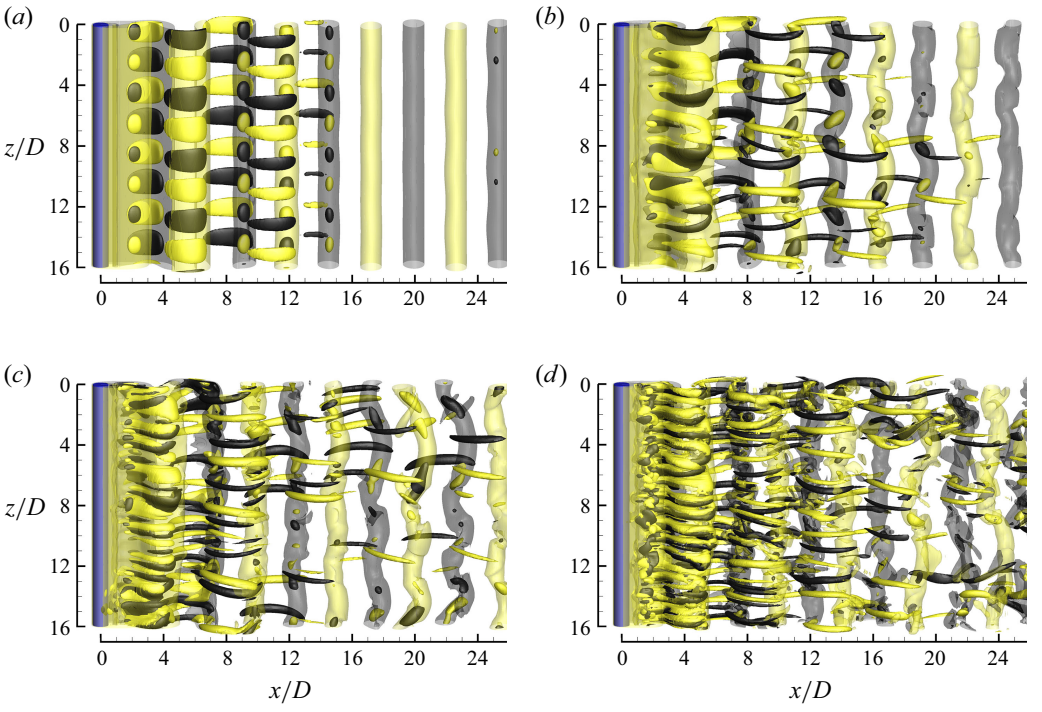

Figure 8. Instantaneous vorticity fields for $L/D = 0.5$: (*a*) $Re = 220$ (ordered mode A structure before evolution to dislocations), (*b*) $Re = 220$ (disordered mode A structure in the fully developed flow), (*c*) $Re = 260$ (disordered finer-scale structure) and (*d*) $Re = 400$ (increasingly disordered finer-scale structure). The translucent iso-surfaces represent spanwise vortices with $|\omega_z| = 0.5$, while the opaque iso-surfaces represent streamwise vortices with $|\omega_x| = 0.07$, 0.7, 0.7 and 1.0 for panels (*a–d*), respectively. Dark grey and light yellow denote positive and negative vorticity values, respectively. The flow is from left to right past the cylinder on the left.

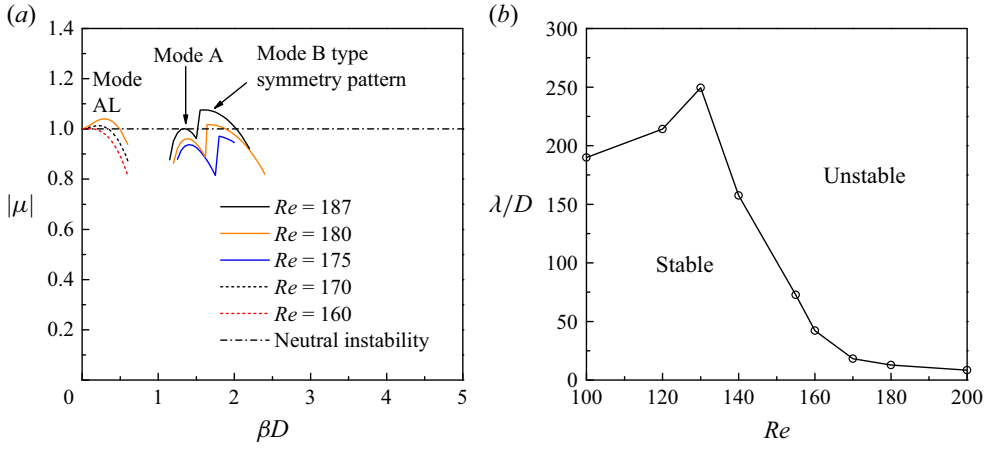

Figure 9. Floquet analysis results for $L/D = 1$: (*a*) the $|\mu|$–β relationships for several Re values, and (*b*) the neutral instability curve for mode AL.

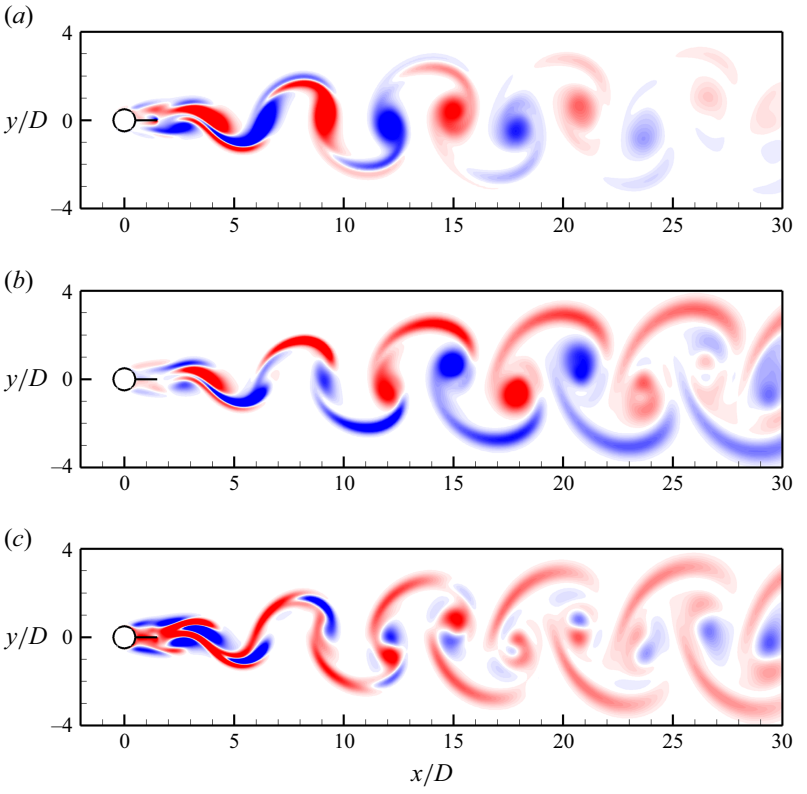

Figure 10. Streamwise perturbation vorticity fields for the case $(L/D, Re) = (1, 180)$: (*a*) mode AL predicted at $\beta D = 0.3$, (*b*) mode A predicted at $\beta D = 1.44$ and (*c*) a synchronous mode of mode B type symmetry pattern predicted at $\beta D = 1.68$. Red and blue denote positive and negative vorticity values, respectively.

multiple modes rather than a single mode, and (ii) the 2-D base flow becomes aperiodic at $Re > 240$, which prohibits a strict Floquet analysis.

To reveal complex mode interactions in the real 3-D flows, 3-D DNSs are performed with $L_z/D = 32$. Although the onset of three-dimensionality is well below $Re = 100$, the 3-D DNSs are performed for $Re \geq 180$, because

(i) In addition to mode AL, other modes identified by the Floquet analysis become unstable at $Re \gtrsim 180$ (figure 9*a*). Therefore, in the real 3-D flow, mode interactions may be expected at $Re \gtrsim 180$.
(ii) With the increase in Re, the critical λ/D for the mode AL instability decreases significantly (figure 9*b*), such that a reduced L_z may be used for the DNS. At $Re = 180$, the critical λ/D for the mode AL instability ($= 12.8$) is well below $L_z/D = 32$ used for the DNS. The adequacy of $L_z/D = 32$ for the present DNS is validated in table 5 by an L_z dependence study at $Re = 180$.

Figure 11 illustrates the wake structures predicted by the 3-D DNS with $L_z/D = 32$. At $Re = 180$, the wake is represented by one spanwise period of mode AL (figure 11*a*). The periodicity of the mode AL structure is confirmed by an additional 3-D DNS with $L_z/D = 64$, where two spanwise periods of mode AL are observed (not shown). With the increase in Re to 190, a mixture of mode AL and the smaller-scale mode A (e.g. over $z/D \sim 16$–21 in figure 11*b*) is observed. The emergence of mode A in the real 3-D flow is

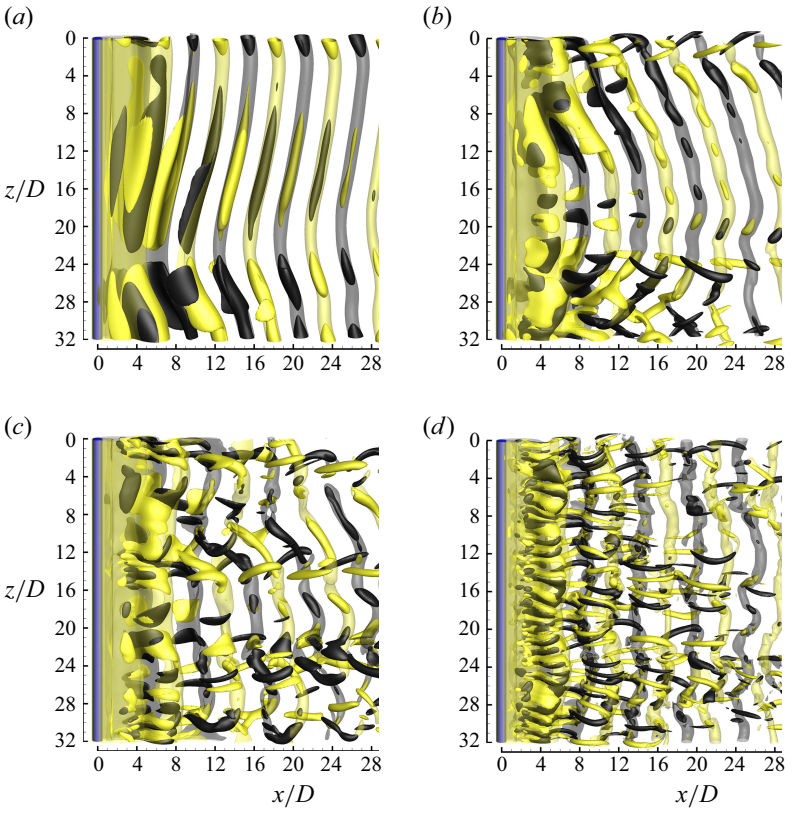

Figure 11. Instantaneous vorticity fields for $L/D = 1$: (*a*) $Re = 180$ (one spanwise period of mode AL), (*b*) $Re = 190$ (a mixture of modes AL and A), (*c*) $Re = 200$ (disappearance of mode AL) and (*d*) $Re = 280$ (chaotic fine-scale structures). The translucent iso-surfaces represent spanwise vortices with $|\omega_z| = 0.5$, while the opaque iso-surfaces represent streamwise vortices with $|\omega_x| = 0.15$, 0.35, 0.4 and 0.7 for panels (a–d), respectively.

consistent with the mode A instability predicted by the Floquet analysis at the critical *Re* of 186.8. With the further increase in *Re* to 200 and beyond, mode AL is no longer observed. The wake is dominated by disordered smaller-scale ($\lambda/D \sim 5$) mode A type structures at $Re = 200$ (figure 11*c*) and even finer-scale structures ($\lambda/D \sim 1$) over $Re = 240$–400 (figure 11*d*).

4.3. *Three-dimensional results for L/D = 2–3*

As *L/D* increases from 1 to 2, the onset of three-dimensionality is significantly delayed to $Re_{cr3D} > 320$ (figure 4*a*). For $L/D = 2$ and 3, mode BL is the only unstable mode up to at least $Re = 400$, and its neutral instability curve is presented in figure 12(*b*). Figure 12(*a*) also reveals a marginally stable mode for $L/D = 2$ (not observed for $L/D = 3$). Based on a curve fitting of the peak $|\mu|$ values for $Re = 300$–360, the largest $|\mu|$ value for this mode, i.e. $|\mu| = 0.998$ at $Re = 331$, is confirmed to be less than 1.0.

Figure 13 shows the streamwise perturbation vorticity fields for mode BL and the stable mode. The symmetry pattern for mode BL (figure 13*a*) is similar to that of the conventional mode B observed for $L/D = 0$–0.5 (e.g. figure 6*d*). However, mode BL differs from mode B in that (i) its spanwise wavelength is more than ten times larger than that for mode B (figure 4*b*), and (ii) the neighbouring streamwise vortices along the streamwise direction

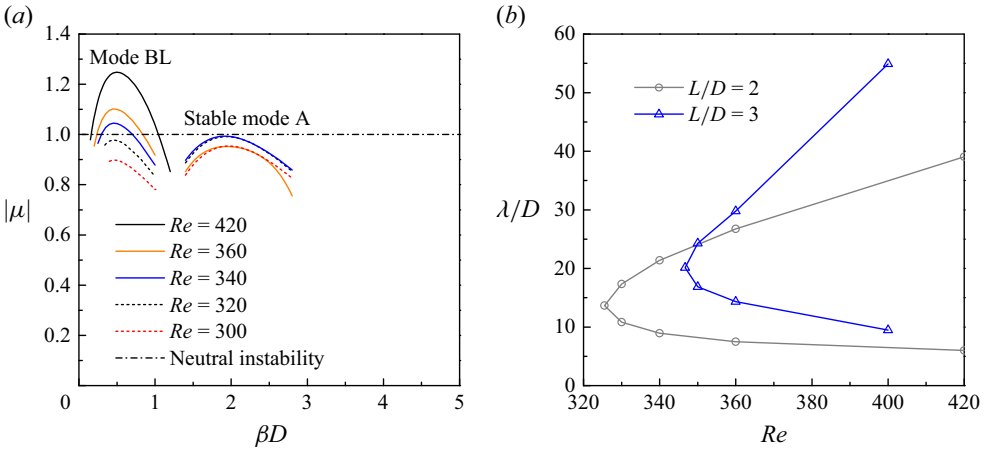

Figure 12. Floquet analysis results for $L/D = 2$ and 3: (*a*) the $|\mu|$–β relationships for $L/D = 2$, and (*b*) the neutral instability curves for the 3-D wake instability mode, i.e. mode BL.

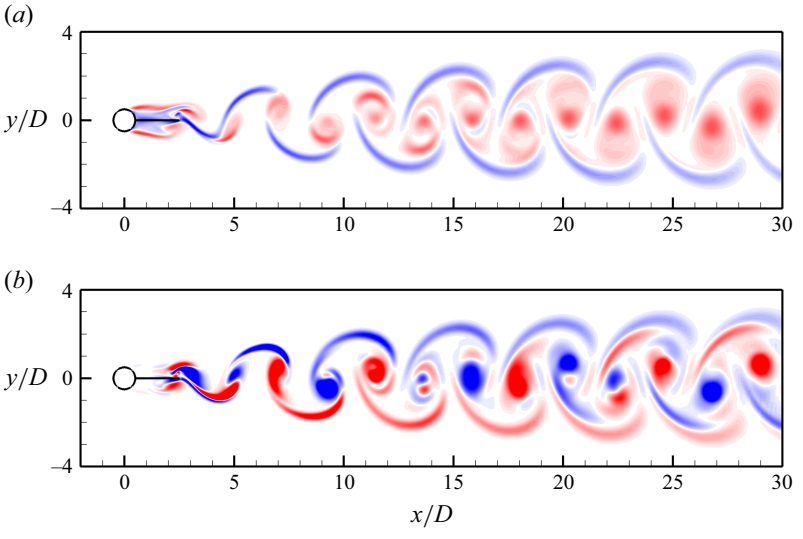

Figure 13. Streamwise perturbation vorticity fields for the case $(L/D, Re) = (2, 330)$: (*a*) mode BL predicted at $\beta D = 0.4$, and (*b*) mode A predicted at $\beta D = 2.0$. Red and blue denote positive and negative vorticity values, respectively.

are disconnected (figure 13*a*). As for the stable mode shown in figure 13(*b*), its pattern resembles that of the conventional mode A (figure 6*a*), such that it is termed stable mode A in figure 12(*a*). It is also noticed in figure 13 that the 3-D modes are mainly developed based on the interactions of the neighbouring primary vortices that occur downstream of the splitter plate, rather than based on the primary vortices initially generated on the two sides of the plate. This phenomenon may contribute to the delayed 3-D wake transition for $L/D \geq 2$, as the strength of the primary vortices decays with distance downstream.

Figure 14 illustrates the overall wake structures for $L/D = 2$ predicted by the 3-D DNS with $L_z/D = 32$. For Re slightly above the Re_{cr3D} of 325.5, e.g. at $Re = 330$, nine spanwise periods of the stable mode A structure are observed at the initial stage of the simulation (figure 14*a*). The spanwise wavelength of the stable mode A structure is approximately

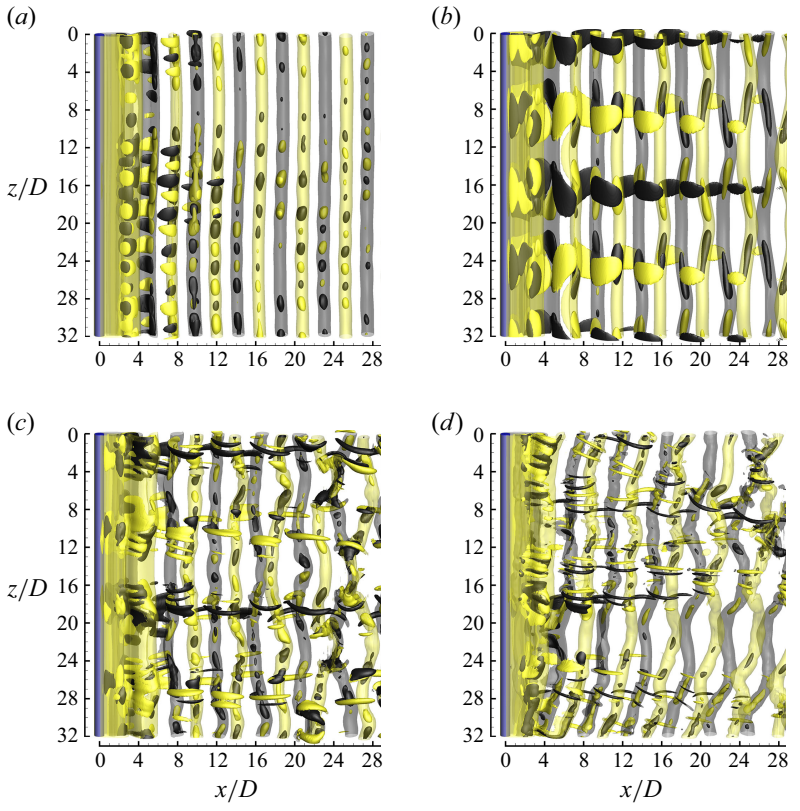

Figure 14. Instantaneous vorticity fields for $L/D = 2$: (*a*) $Re = 330$ (stable mode A structure before evolution to mode BL), (*b*) $Re = 330$ (ordered mode BL structure in the fully developed flow), (*c*) $Re = 400$ (disordered mode BL structure) and (*d*) $Re = 480$ (chaotic fine-scale structures). The translucent iso-surfaces represent spanwise vortices with $|\omega_z| = 0.5$, while the opaque iso-surfaces represent streamwise vortices with $|\omega_x| = 0.08$, 0.2, 0.5 and 1.0 for panels (a–d), respectively.

3.6*D*, which is close to the most unstable wavelength predicted by the Floquet analysis (i.e. 3.3*D* at $Re = 330$). With the evolution in time, the stable mode A structure decays gradually. The gradual decay of the stable mode A structure over the initial stage is also observed for $Re = 320$ ($<Re_{cr3D}$), which indicates that the stable mode A structure is triggered by the initial disturbance prescribed in the domain for the generation of flow three-dimensionality. Since the stable mode A is marginally stable (figure 12*a*), it may be triggered by the initial disturbance but cannot persist indefinitely. As shown in figure 14(*b*), the fully developed wake for $Re = 330$ is represented by two spanwise periods of ordered mode BL structure, because mode BL is the only unstable mode (figure 12*a*). As *Re* increases to 360, 400 and 440, the mode BL structure becomes increasingly disordered (e.g. figure 14*c*), yet the symmetry pattern of mode BL is still visible. With the further increase in *Re* to 480, the mode BL structure is no longer visible, and the wake is represented by chaotic finer-scale structures (figure 14*d*).

4.4. *Three-dimensional results for L/D = 4–6*

While mode BL dominates the 3-D wake patterns for $L/D = 2$–3, it becomes a marginally stable mode for $L/D = 4$ (figure 15*a*), and is no longer detected for $L/D = 5$ and 6 (omitted for brevity). For the mode BL peak observed in figure 15(*a*), a curve fitting of

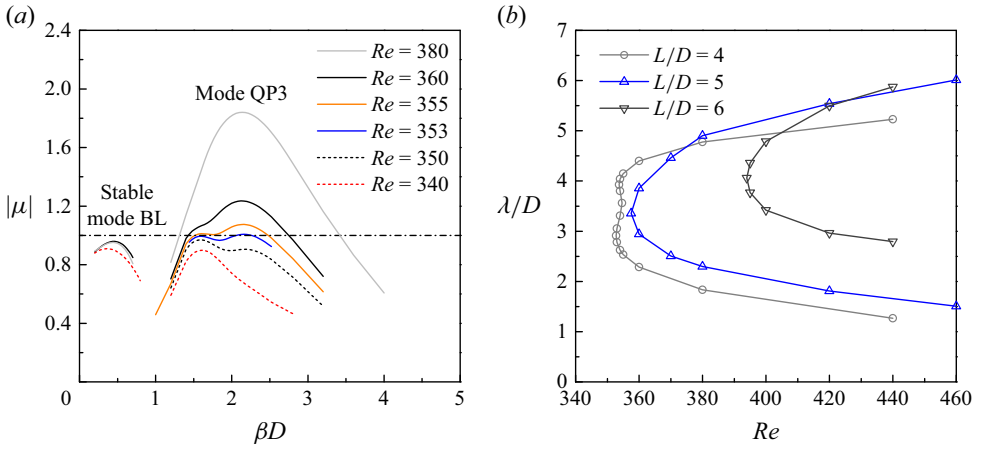

Figure 15. Floquet analysis results for $L/D = 4$–6: (a) the $|\mu|$–β relationships for $L/D = 4$, and (b) the neutral instability curves for the 3-D wake instability mode, i.e. mode QP3.

the peak $|\mu|$ values for $Re = 340$–400 indicates that the most unstable condition occurs at $Re = 368$, with the largest $|\mu|$ value of 0.97, which confirms that mode BL is now stable. For $L/D = 4$–6, the only unstable mode up to at least $Re = 440$ is a QP mode called QP3, and its neutral instability curve is presented in figure 15(*b*).

Figure 16 shows the 3-D DNS results for $L/D = 4$, where the 3-D wake pattern is now dominated by mode QP3. For Re slightly above the Re_{cr3D} of 352.8, e.g. at $Re = 360$, six relatively ordered spanwise periods of the mode QP3 structure are observed in the fully developed flow (figure 16*a*). The spanwise wavelength of the mode QP3 structure is approximately $2.7D$, which is close to the most unstable wavelength predicted by the Floquet analysis (i.e. $2.9D$ at $Re = 360$). With the further increase in Re over 360–480, the mode QP3 structure becomes increasingly disordered (figure 16).

4.5. *Summary of the 3-D wake transition process*

The Floquet analysis and 3-D DNS results presented in §§ 4.1 to 4.4 reveal significantly different 3-D unstable modes and wake structures for different L/D conditions. Nevertheless, the 3-D wake transition processes for different L/D conditions share some general similarities. Specifically, over a certain range of Re above the Re_{cr3D} value, the real 3-D flow is dominated by the first unstable mode predicted by the Floquet analysis, which is reasonable. With the increase in Re, the spanwise wavelength of the wake structure gradually decreases, and the wake structure becomes increasingly chaotic. This process is realised through either emergence of additional finer-scale unstable modes in the 3-D flow (e.g. $L/D = 0.5$ and 1), or progressive irregularity and breakdown of the modal structure itself (e.g. $L/D \geq 2$). In any case, the wake is dominated by chaotic small-scale structures (with $\lambda/D \lesssim 1$) at the largest Re simulated in this study, and the wake is expected to become increasingly chaotic and turbulent with further increase in Re.

Over the wake transition process from two to three dimensions and eventually to chaos and turbulence, the monotonic decrease in the spanwise wavelength of the 3-D wake structures with increasing Re appears to be a common phenomenon in various bluff-body flows. Other than the present scenarios, this phenomenon is also observed for the flow around a circular cylinder (Jiang *et al.* 2016), a square cylinder with various incidence angles (Yoon, Yang & Choi 2012; Jiang, Cheng & An 2018; Jiang 2021), a rectangular cylinder with various cross-sectional aspect ratios (Ju & Jiang 2024), etc.

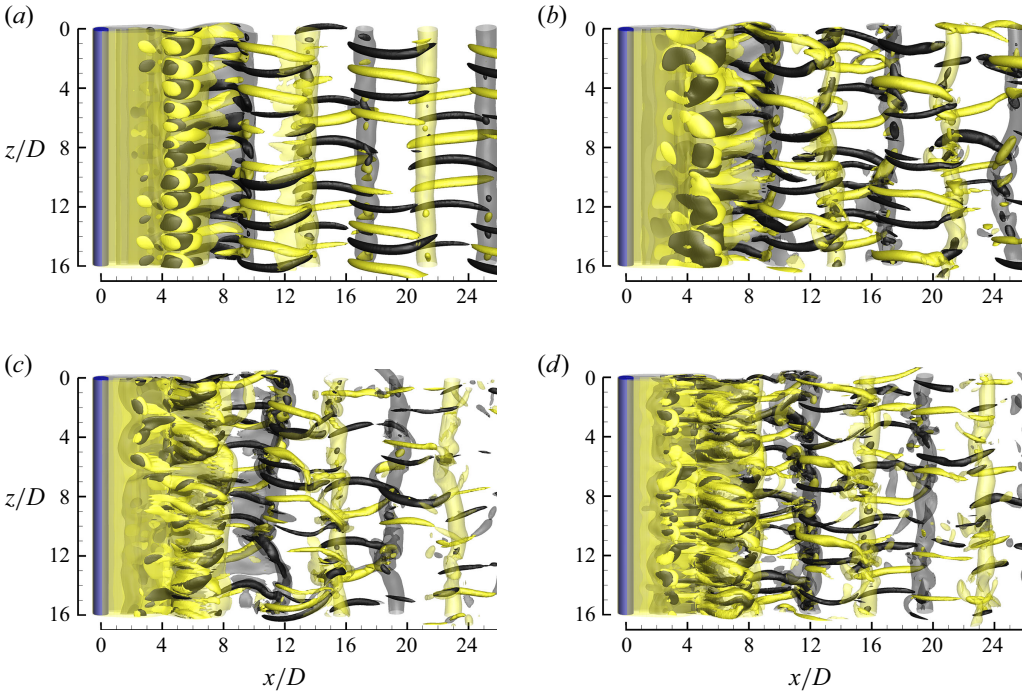

Figure 16. Instantaneous vorticity fields for $L/D = 4$: (*a*) $Re = 360$, (*b*) $Re = 380$, (*c*) $Re = 420$ and (*d*) $Re = 480$. The translucent iso-surfaces represent spanwise vortices with $|\omega_z| = 0.5$, while the opaque iso-surfaces represent streamwise vortices with $|\omega_x| = 0.3$, 0.6, 1.0 and 1.0 for panels (*a–d*), respectively.

This phenomenon suggests that, with the increase in *Re*, new unstable Floquet modes with decreasing (rather than increasing) spanwise wavelengths are much more likely to be actually manifested in the real 3-D flow. Eventually, the small-scale 3-D wake structures become increasingly chaotic with increasing *Re*, which facilitates evolution of turbulence in the wake.

4.6. *Variations in the hydrodynamic forces*

The effects of flow three-dimensionality on the hydrodynamic forces are reflected by a comparison of the forces computed by the 2-D and 3-D DNSs. Figure 17(*a*,*b*) shows the mean drag and fluctuating lift on the cylinder for various *L/D* conditions. For the cases with a splitter plate (i.e. $L/D \geq 0.5$), the mean drag is hardly affected by the flow three-dimensionality, while the fluctuating lift is affected to a greater extent. This is because the fluctuating lift is completely induced by the alternate formation of the low pressure regions in the near wake, such that it is more sensitive to the influence of the flow three-dimensionality on the low pressure regions.

The effects of flow three-dimensionality on the fluctuating lift on the cylinder are examined in detail. As shown in figure 17(*b*), for $L/D = 0.5$ and 1, the flow three-dimensionality has a strong effect in reducing the fluctuating lift. In general, this effect increases with increasing *Re*, because the increasingly finer-scale and chaotic 3-D wake structures result in an increased degree of flow three-dimensionality. For $L/D \geq 2$, however, the effect of flow three-dimensionality on the lift reduction becomes rather weak (the lift reduction induced by the flow three-dimensionality is less than 10 % of that induced by the alteration of the 2-D flow by the splitter plate). With the increase in *L/D* from

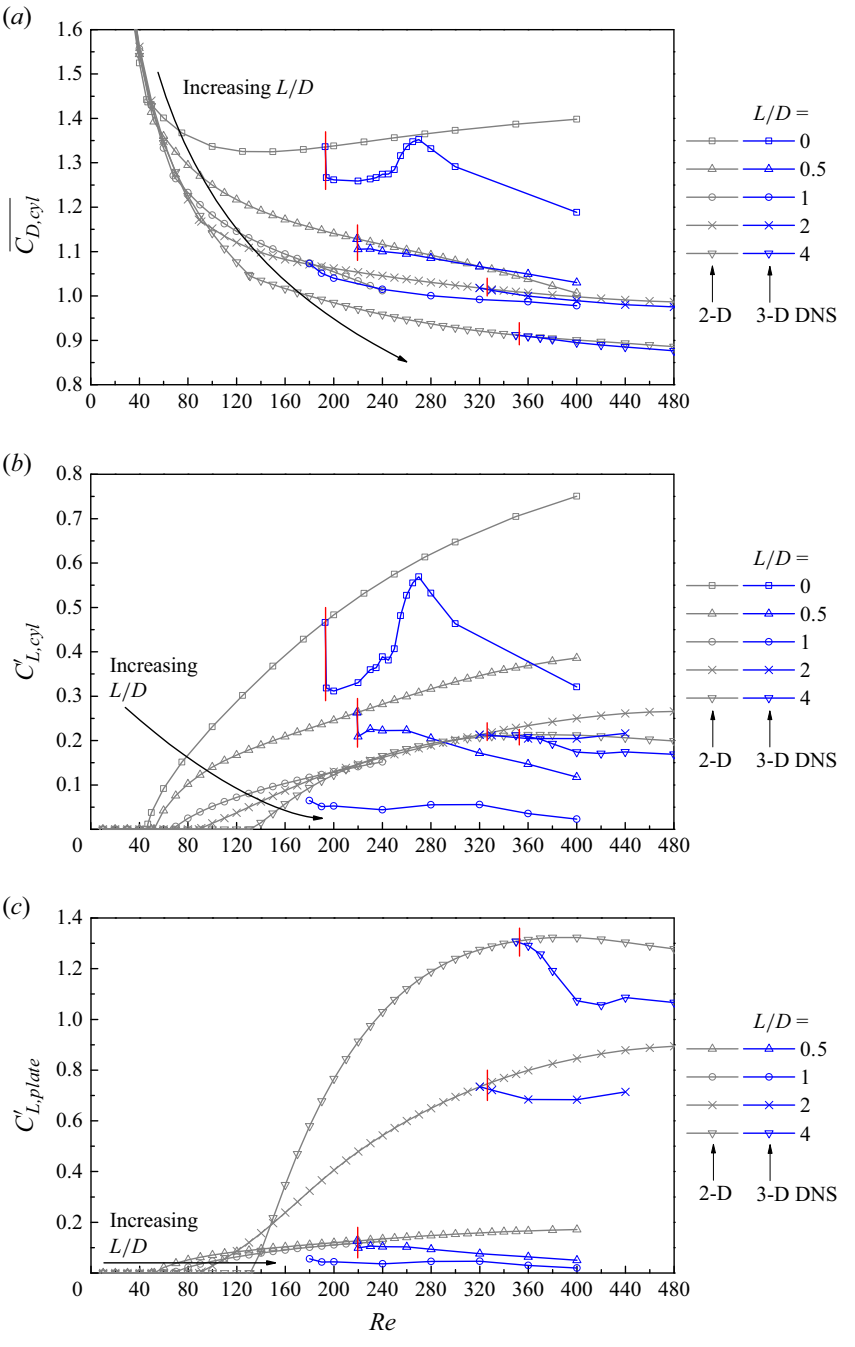

Figure 17. Hydrodynamic coefficients computed by the 2-D and 3-D DNSs, including the (*a*) $\overline{C_{D,cyl}} - Re$, (*b*) $C'_{L,cyl} - Re$ and (*c*) $C'_{L,plate} - Re$ relationships. For each L/D condition (apart from $L/D = 1$), the Re_{cr3D} value is indicated by a red vertical bar.

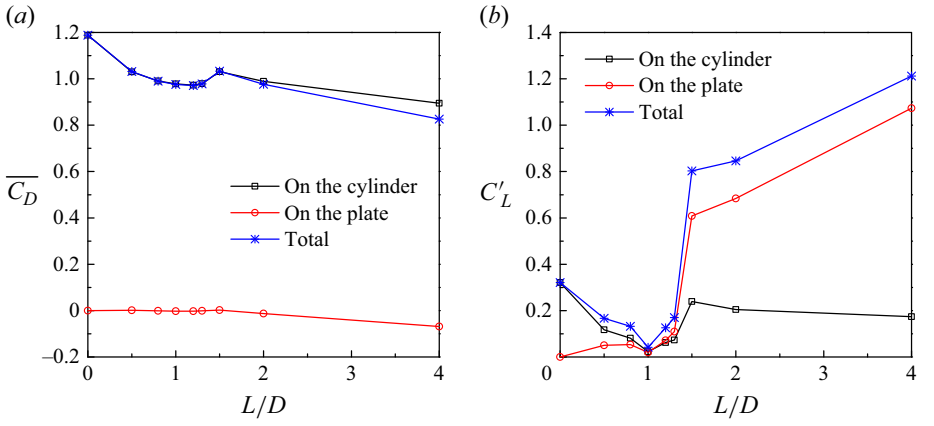

Figure 18. Hydrodynamic coefficients computed by the 3-D DNS at $Re = 400$: (*a*) the mean drag coefficient, and (*b*) the root-mean-square lift coefficient.

1 to 2, the streamwise location for the formation of the primary vortices moves from downstream of the splitter plate to the two sides of the plate. Nevertheless, the 3-D wake structures are destabilised downstream of the plate based on the interaction of the primary vortices of opposite signs (figure 13). Therefore, the low pressure regions, which govern the fluctuating lift on the cylinder, are mainly shaped by the formation of the primary vortices on the two sides of the plate, and are relatively less affected by the flow three-dimensionality developed further downstream (in contrast to $L/D \leq 1$ where the primary vortices and the 3-D wake structures are both developed downstream of the plate).

For $L/D \leq 1$, in addition to the relatively strong contribution of the 3-D wake structures on the lift reduction, the relatively small Re_{cr3D} values also contribute to an early start (in terms of Re) for the influence of flow three-dimensionality on the lift reduction, such that, when compared at the same Re value, relatively large lift reductions are observed for $L/D \leq 1$. For example, after taking into account the 3-D effects, $L/D = 0.5$ may even outperform $L/D = 4$ in the lift reduction (and the associated suppression/mitigation of the VIV and acoustic noise).

Figure 17(*c*) examines the fluctuating lift on the plate. For each 3-D case, the flow three-dimensionality results in almost identical percentage reductions in the fluctuating lift on the cylinder and the plate. A combination of figure 17(*b*,*c*) suggests that the use of a plate of $L/D = 1$ may suppress the fluctuating lift on the cylinder–plate system almost completely.

To reveal this optimal suppression more clearly, figure 18 shows the mean drag and fluctuating lift coefficients computed by the 3-D DNS at a fixed Re of 400. The minimum fluctuating lift is indeed observed at $L/D = 1$ (figure 18*b*). For $L/D \sim 0.5$–1.3, the fluctuating lift remains at a relatively small level, and the mean drag also displays a local trough, which suggests good performance of the splitter plate over this range of L/D.

4.7. *Hysteresis effect at the onset of three-dimensionality*

The existence or absence of a hysteresis effect at the onset of three-dimensionality may be identified by several methods, as summarised in table 6. With the availability of the 3-D hydrodynamic forces shown in figure 17, the simplest method (method 1 in table 6) is to identify the sudden or gradual variation in the 3-D forces at Re_{cr3D}. A sudden variation in the forces arises from a sudden increase in the degree of three-dimensionality at Re_{cr3D} due to a specific 3-D wake instability mode, which corresponds to a subcritical instability (hysteretic condition) of the flow (Jiang *et al.* 2018). In contrast, a gradual variation in the

Method	$L/D = 0$ and 0.5	$L/D = 2$	$L/D = 4$
1. Based on sudden or gradual variation in the forces at Re_{cr3D}	Hysteretic	Non-hysteretic	Non-hysteretic
2. Based on direct 3-D DNS of the decreasing Re branch	Hysteretic	Non-hysteretic	Non-hysteretic
3. Based on the use of Landau equation	Hysteretic	Hysteretic (incorrect)	Non-hysteretic

Table 6. Hysteresis effect at the onset of three-dimensionality identified by different methods.

forces at Re_{cr3D} corresponds to a supercritical instability (non-hysteretic condition) of the flow (Jiang *et al.* 2018). As shown in figure 17, sudden variations in the forces at Re_{cr3D} are observed for $L/D = 0$ and 0.5, which indicates that the corresponding mode A instability is subcritical (hysteretic). In contrast, gradual variations in the forces at Re_{cr3D} are observed for $L/D = 2$ and 4, which indicates that the corresponding modes BL and QP3 instabilities, respectively, are both supercritical (non-hysteretic).

The hysteresis effect can also be confirmed by additional 3-D DNS of the decreasing Re branch (method 2 in table 6), where a fully developed flow field with Re slightly above Re_{cr3D} is employed as the initial condition, and additional DNSs with a stepwise decrease in Re can reveal the critical Re below which the wake transitions back to two-dimensional. To minimise the computational cost for this set of DNSs, the spanwise domain length L_z may be set to the most unstable spanwise wavelength of the first 3-D wake instability mode, such that only one spanwise period of the 3-D mode is resolved. For $L/D = 0.5$, the initial condition for the additional 3-D DNS is a spanwise period of the mode A structure obtained at $Re = 220$ ($> Re_{cr3D} = 219.6$), and a stepwise decrease in Re at an interval of 1 reveals the critical Re of 214 for the 3-D-to-2-D transition, which confirms that the mode A instability is hysteretic. In contrast, the initial conditions of a spanwise period of mode BL structure for $L/D = 2$ at $Re = 326$ ($> Re_{cr3D} = 325.5$) and a spanwise period of mode QP3 structure for $L/D = 4$ at $Re = 353.5$ ($> Re_{cr3D} = 352.8$) both decay to two dimensions after a decrease in Re by 1, which confirms that the modes BL and QP3 instabilities are non-hysteretic.

The Landau equation (Landau & Lifshitz 1976) (method 3 in table 6) is also commonly used in the literature for the identification of the hysteresis effect (e.g. Dušek, Le Gal & Fraunié 1994; Henderson & Barkley 1996; Thompson, Leweke & Provansal 2001; Sheard, Thompson & Hourigan 2004; Carmo *et al.* 2008). For the amplitude $A(t)$ of a 3-D perturbation mode, the Landau equation can be written up to third order as

$$\frac{\mathrm{d}A}{\mathrm{d}t} = (\sigma + \mathrm{i}\omega)\, A - l\,(1 + \mathrm{i}c)\,|A|^2\, A + \ldots, \tag{4.4}$$

where σ is the linear growth rate of the perturbation, ω is the angular oscillation frequency during the linear growth phase and c is the Landau constant. The l-coefficient is determined by plotting $\mathrm{d}(\log|A|)/\mathrm{d}t$ against $|A|^2$, where the slope of the curve near $|A|^2 = 0$ gives $-l$. The hysteresis of the wake instability mode is determined based on the sign of the l-coefficient, where a positive l corresponds to a non-hysteretic flow, while a negative l corresponds to a hysteretic flow. More details on this method can be found in Dušek *et al.* (1994), Sheard *et al.* (2004) and Carmo *et al.* (2008).

In the present study, the Landau equation is applied to the cases with Re slightly above Re_{cr3D} and L_z close to the most unstable spanwise wavelength of the first 3-D wake instability mode, i.e. (L/D, Re, L_z) = (0.5, 220, 4) for mode A, (2, 327, 13.67) for mode BL and (4, 355, 2.91) for mode QP3. Figure 19(*a–c*) shows the time evolution of the mode

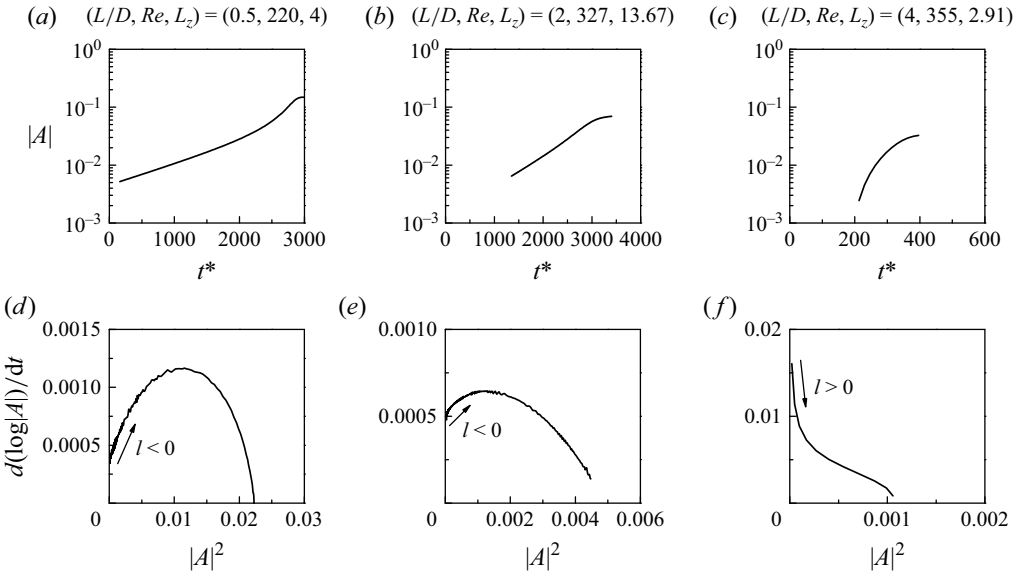

Figure 19. Identification of the hysteresis effect using the Landau equation: (*a*) time evolution of the mode amplitude |*A*| for the case (L/D, Re, L_z) = (0.5, 220, 4), (*b*) time evolution of |*A*| for the case (L/D, Re, L_z) = (2, 327, 13.67), (c) time evolution of |*A*| for the case (L/D, Re, L_z) = (4, 355, 2.91) and (*d–f*) the [$d(\log|A|)/dt$] –$|A|^2$ relationships for the corresponding cases shown in panels (*a–c*), respectively.

amplitude |*A*|, which is measured from the envelope of the fluctuation of the spanwise velocity sampled at (x/D, y/D) = (5, 1) and a z/D within the 3-D mode structure. Based on the corresponding l-coefficient determined from figure 19(*d–f*), the cases with $L/D = 0.5$, 2 and 4 are deemed hysteretic, hysteretic and non-hysteretic, respectively.

As summarised in table 6, the three methods lead to consistent conclusions for the cases with $L/D = 0$, 0.5 and 4, but discrepancies for the case with $L/D = 2$. We believe that the error lies in the use of the Landau equation for the case with (L/D, Re, L_z) = (2, 327, 13.67). For this case, the flow is initialised with several spanwise periods of the marginally stable mode A (figure 12*a*) structure, followed by the dominance of a spanwise period of the unstable mode BL (figure 12*a*) structure at $t^* \gtrsim 1000$ (similar to the flow evolution shown in figure 14*a*,*b*). Although the Landau equation is applied to the time range of $t^* \gtrsim 1350$ (figure 19*b*), which corresponds to the dominance of the unstable mode BL only, the time evolution of |*A*| may still be contaminated by the initial development of the stable mode A and lead to a false conclusion on the existence of hysteresis. In comparison, methods 1 and 2 are based on the fully developed flow only, and are thus unaffected by the initial transients.

5. Conclusions

This paper investigates the 2-D and 3-D wake transitions, 3-D wake instability modes, 3-D wake structures and 2-D and 3-D hydrodynamic characteristics for a circular cylinder with a rear-attached splitter plate, over a parameter space of $Re = 10$–480 and $L/D = 0$–6.

With the increase in L/D, the Re_{cr2D} value increases monotonically. This is because when the vortex shedding is forced to occur further downstream by the increase in L/D, the separating shear layers at the location of vortex shedding are further weakened by (i) the elongation of the separating shear layers, and (ii) the shear layers developed on the

two sides of the no-slip plate. Therefore, an increased Re is required for the separating shear layers to gain more strength to roll up into vortices.

The Re_{cr3D} value and the 3-D unstable modes and structures are also significantly altered by the splitter plate. Compared with $Re_{cr3D} = 189.8$ for an isolated cylinder, the onset of three-dimensionality is brought forward to $Re_{cr3D} < 100$ for $L/D = 1$ and significantly delayed to $Re_{cr3D} > 320$ for $L/D = 2$–6. With the increase in L/D, the first 3-D unstable mode/structure changes in the sequence of (i) mode A for $L/D = 0$–0.5, (ii) mode AL for $L/D = 1$, (iii) mode BL for $L/D = 2$–3 and (iv) mode QP3 for $L/D = 4$–6. For each L/D category, the 3-D wake transition process and mode interactions are revealed by the DNSs. A general similarity is that the spanwise wavelength of the 3-D wake structures decreases monotonically with increasing Re, which is realised through either emergence of additional finer-scale unstable modes in the 3-D flow (e.g. $L/D = 0.5$ and 1), or progressive irregularity and breakdown of the modal structure itself (e.g. $L/D \geq 2$). Eventually, the small-scale 3-D wake structures become increasingly chaotic with increasing Re, which facilitates evolution of turbulence in the wake.

The strong influence of the splitter plate on the formation of the primary vortices and 3-D wake structures alter the hydrodynamic characteristics strongly. In particular, optimal lift reduction is achieved at $L/D \sim 1$ (rather than at very large L/D), and its physical reason is explained based on the spanwise and streamwise wake structures and the Re_{cr3D} values examined in this study.

At the onset of three-dimensionality, a hysteresis effect is identified for the mode A instability for $L/D = 0$ and 0.5, but not for the modes BL and QP3 instabilities for $L/D = 2$ and 4, respectively. In addition, we discussed strength and limitation of the three methods for the identification of the hysteresis effect (based on (i) sudden or gradual variation in the forces at Re_{cr3D}, (ii) direct 3-D DNS of the decreasing Re branch and (iii) the use of Landau equation). The first two methods draw conclusion from the fully developed flow only, whereas the third method may be contaminated by initial transients induced by stable Floquet modes and may thus lead to a false conclusion on the existence/absence of hysteresis.

Funding. H.J. would like to acknowledge support from National Natural Science Foundation of China (Grant No. 52301341).

Declaration of interests. The author reports no conflict of interest.

Appendix A. Method for the determination of Re_{cr2D}

For each L/D condition, the Re_{cr2D} is determined by the following three steps: (i) computing the cases near the Re_{cr2D} at an interval of $\Delta Re = 1$, (ii) calculating the exponential growth/decay rate of the amplitude of C_L for the two cases immediately before and after the instability and (iii) determining the Re_{cr2D} at neutral instability (i.e. zero growth/decay rate) through linear interpolation of the growth/decay rates.

For example, figure 20 shows time histories of C_L for $L/D = 0.5$ and $Re = 52$ and 53, where the amplitude of C_L displays exponential decay and exponential growth, respectively. This feature suggests that Re_{cr2D} is within $Re = 52$–53. To determine the precise value of Re_{cr2D}, the growth/decay rate of the amplitude of C_L is quantified. Specifically, the upper and lower envelopes of the time history of C_L are each fitted with an exponential function

$$C_L = A \exp(Bt^*) + C, \tag{A1}$$

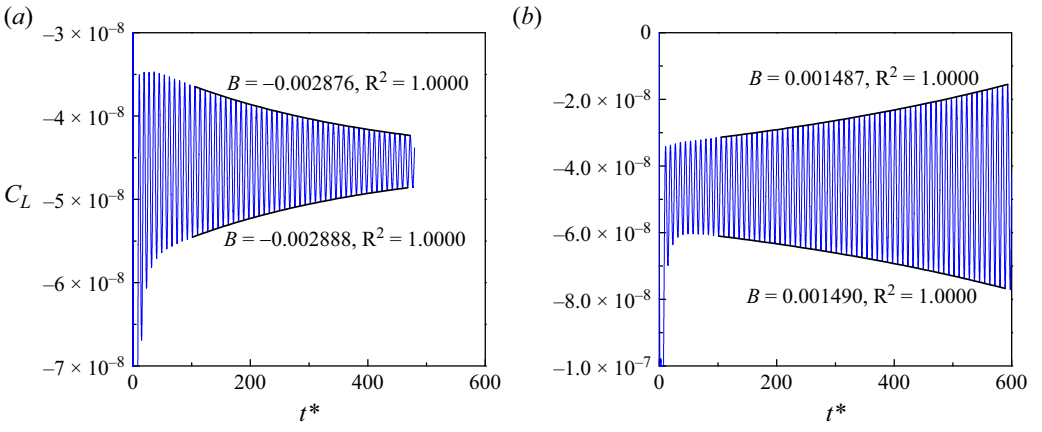

Figure 20. Time history of C_L for $L/D = 0.5$ and (*a*) $Re = 52$, and (*b*) $Re = 53$. The black curves show exponential fitting of the upper and lower envelopes.

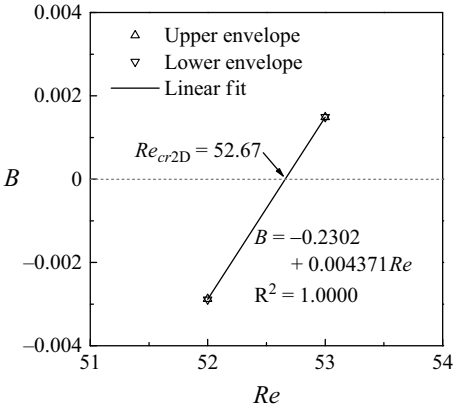

Figure 21. Relationship between the growth/decay rate and the Reynolds number.

where A, B and C are curve fitting coefficients. After discarding the initial transients of $t^* < 100$, the coefficient of determination (denoted R^2) for the fitted curves is 1.0000, which suggests perfect exponential fitting. Based on the growth/decay rates B obtained at $Re = 52$ and 53, figure 21 shows a linear fit of the B–Re relationship. The precise value of Re_{cr2D} (= 52.67) can be determined at the zero growth/decay rate ($B = 0$).

It is worth noting that at Re close to Re_{cr2D}, the fully developed flow with vortex shedding may be established after time evolution of a long period (with $t^* > 10^4$), which requires a significant computational cost. The merit of the present method is that it does not require vortex shedding to be visualised. The precise Re_{cr2D} value can be determined at t^* well within 10^3.

References

Ali, M.S.M., Doolan, C.J. & Wheatley, V. 2011 Low Reynolds number flow over a square cylinder with a splitter plate. *Phys. Fluids* **23**, 033602.

Anderson, E.A. & Szewczyk, A.A. 1997 Effects of a splitter plate on the near wake of a circular cylinder in 2 and 3-dimensional flow configurations. *Exp. Fluids* **23**, 161–174.

APELT, C.J., WEST, G.S. & SZEWCZYK, A.A. 1973 The effects of wake splitter plates on the flow past a circular cylinder in the range $10^4 < R < 5 \times 10^4$. *J. Fluid Mech.* **61**, 187–198.

APELT, C.J. & WEST, G.S. 1975 The effects of wake splitter plates on bluff-body flow in the range $10^4 < R < 5 \times 10^4$. Part 2. *J. Fluid Mech.* **71**, 145–160.

BARKLEY, D. & HENDERSON, R.D. 1996 Three-dimensional Floquet stability analysis of the wake of a circular cylinder. *J. Fluid Mech.* **322**, 215–241.

Bearman 1965 Investigation of the flow behind a two-dimensional model with a blunt trailing edge and fitted with splitter plates. *J. Fluid Mech.* **21** (02), 241–255.

BLACKBURN, H.M., MARQUES, F. & LOPEZ, J.M. 2005 Symmetry breaking of two-dimensional time-periodic wakes. *J. Fluid Mech.* **522**, 395–411.

CANTWELL, C.D., *et al.* 2015 Nektar++: an open-source spectral/hp element framework. *Comput. Phys. Commun.* **192**, 205–219.

CARBERRY, J., SHERIDAN, J. & ROCKWELL, D. 2005 Controlled oscillations of a cylinder: forces and wake modes. *J. Fluid Mech.* **538**, 31–69.

CARMO, B.S., SHERWIN, S.J., BEARMAN, P.W. & WILLDEN, R.H.J. 2008 Wake transition in the flow around two circular cylinders in staggered arrangements. *J. Fluid Mech.* **597**, 1–29.

CARMO, B.S., MENEGHINI, J.R. & SHERWIN, S.J. 2010 Secondary instabilities in the flow around two circular cylinders in tandem. *J. Fluid Mech.* **644**, 395–431.

CHAUHAN, M.K., DUTTA, S., MORE, B.S. & GANDHI, B.K. 2018 Experimental investigation of flow over a square cylinder with an attached splitter plate at intermediate reynolds number. *J. Fluid. Struct.* **76**, 319–335.

CHOI, H., JEON, W.P. & KIM, J. 2008 Control of flow over a bluff body. *Annu. Rev. Fluid Mech.* **40** (1), 113–139.

CHUTKEY, K., SURIYANARAYANAN, P. & VENKATAKRISHNAN, L. 2018 Near wake field of circular cylinder with a forward splitter plate. *J. Wind Engng. Ind. Aerodyn.* **173**, 28–38.

CUI, G.P., FENG, L.H. & HU, Y.W. 2022 Flow-induced vibration control of a circular cylinder by using flexible and rigid splitter plates. *Ocean Eng.* **249**, 110939.

DE ARAUJO, L.A., SCHETTINI, E.B.C. & SILVESTRINI, J.H. 2018 Direct numerical simulation of the flow around a cylinder with splitter plate: analysis for moderated Reynolds numbers. *J. Braz. Soc. Mech. Sci.* **40** (6), 276.

DONG, S., TRIANTAFYLLOU, G.S. & KARNIADAKIS, G.E. 2008 Elimination of vortex streets in bluff-body flows. *Phys. Rev. Lett.* **100** (20), 204501.

DUŠEK, J., LE GAL, P. & FRAUNIÉ, P. 1994 A numerical and theoretical study of the first Hopf bifurcation in a cylinder wake. *J. Fluid Mech.* **264**, 59–80.

DUAN, F. & WANG, J. 2021 Fluid-structure–sound interaction in noise reduction of a circular cylinder with flexible splitter plate. *J. Fluid Mech.* **920**, A6.

FENG, L.H. & WANG, J.J. 2010 Circular cylinder vortex-synchronization control with a synthetic jet positioned at the rear stagnation point. *J. Fluid Mech.* **662**, 232–259.

GAO, D., HUANG, Y., CHEN, W., CHEN, G. & LI, H. 2019 Control of circular cylinder flow via bilateral splitter plates. *Phys. Fluids* **31** (5), 057105.

GERRARD, J.H. 1966 The mechanics of the formation region of vortices behind bluff bodies. *J. Fluid Mech.* **25** (2), 401–413.

HENDERSON, R.D. 1997 Nonlinear dynamics and pattern formation in turbulent wake transition. *J. Fluid Mech.* **352**, 65–112.

HENDERSON, R.D. & BARKLEY, D. 1996 Secondary instability in the wake of a circular cylinder. *Phys. Fluids* **8** (6), 1683–1685.

HWANG, J.Y., YANG, K.S. & SUN, S.H. 2003 Reduction of flow-induced forces on a circular cylinder using a detached splitter plate. *Phys. Fluids* **15** (8), 2433–2436.

JIANG, H. 2021 Three-dimensional wake transition of a diamond-shaped cylinder. *J. Fluid Mech.* **918**, A35.

JIANG, H., CHENG, L. & AN, H. 2017 On numerical aspects of simulating flow past a circular cylinder. *Intl J. Numer. Meth. Fluids* **85** (2), 113–132.

JIANG, H., CHENG, L. & AN, H. 2018 Three-dimensional wake transition of a square cylinder. *J. Fluid Mech.* **842**, 102–127.

JIANG, H., CHENG, L., DRAPER, S., AN, H. & TONG, F. 2016 Three-dimensional direct numerical simulation of wake transitions of a circular cylinder. *J. Fluid Mech.* **801**, 353–391.

JU, X. & JIANG, H. 2024 Two- and three-dimensional wake transitions of a rectangular cylinder and resultant hydrodynamic effects. *J. Fluid Mech.* **989**, A6.

KARNIADAKIS, G.E. 1990 Spectral element-Fourier methods for incompressible turbulent flows. *Comput. Method. Appl. Mech. Engng* **80** (1-3), 367–380.

KARNIADAKIS, G.E., ISRAELI, M. & ORSZAG, S.A. 1991 High-order splitting methods for the incompressible Navier-Stokes equations. *J. Comput. Phys.* **97** (2), 414–443.
KARNIADAKIS, G.E. & SHERWIN, S.J. 2005 *Spectral/Hp Element Methods for CFD*. Oxford University Press.
KOURTA, A., BOISSON, H.C., CHASSAING, P. & HA MINH, H. 1987 Nonlinear interaction and the transition to turbulence in the wake of a circular cylinder. *J. Fluid Mech.* **181**, 141–161.
KWON, K. & CHOI, H. 1996 Control of laminar vortex shedding behind a circular cylinder using splitter plates. *Phys. Fluids* **8** (2), 479–486.
LANDAU, L.D. & LIFSHITZ, E.M. 1976 Mechanics, 3rd edn Pergamon.
MARQUET, O., SIPP, D. & JACQUIN, L. 2008 Sensitivity analysis and passive control of cylinder flow. *J. Fluid Mech.* **615**, 221–252.
OZONO, S. 1999 Flow control of vortex shedding by a short splitter plate asymmetrically arranged downstream of a cylinder. *Phys. Fluids* **11** (10), 2928–2934.
PONCET, P., HILDEBRAND, R., COTTET, G.H. & KOUMOUTSAKOS, P. 2008 Spatially distributed control for optimal drag reduction of the flow past a circular cylinder. *J. Fluid Mech.* **599**, 111–120.
POSDZIECH, O. & GRUNDMANN, R. 2001 Numerical simulation of the flow around an infinitely long circular cylinder in the transition regime. *Theor. Comp. Fluid Dyn.* **15** (2), 121–141.
QIU, Y., SUN, Y., WU, Y. & TAMURA, Y. 2014 Effects of splitter plates and Reynolds number on the aerodynamic loads acting on a circular cylinder. *J. Wind Engng Ind. Aerodyn.* **127**, 40–50.
PRASAD, A. & WILLIAMSON, C.H.K. 1997 A method for the reduction of bluff body drag. *J. Wind Engn Ind. Aerodyn.* **69-71**, 155–167.
ROSHKO, A. 1954 On the drag and shedding frequency of two-dimensional bluff bodies. *NACA Technical Note* **3169**.
ROSHKO, A. 1955 On the wake and drag of bluff bodies. *J. Aeronaut. Sci.* **22** (2), 124–132.
ROSHKO, A. 1961 Experiments on the flow past a circular cylinder at very high Reynolds number. *J. Fluid Mech.* **10** (3), 345–356.
SAHU, T.R., FURQUAN, M. & MITTAL, S. 2019 Numerical study of flow-induced vibration of a circular cylinder with attached flexible splitter plate at low Re. *J. Fluid Mech.* **880**, 551–593.
SERSON, D., MENEGHINI, J.R., CARMO, B.S., VOLPE, E.V. & GIORIA, R.S. 2014 Wake transition in the flow around a circular cylinder with a splitter plate. *J. Fluid Mech.* **755**, 582–602.
SHEARD, G.J., THOMPSON, M.C. & HOURIGAN, K. 2004 From spheres to circular cylinders: non-axisymmetric transitions in the flow past rings. *J. Fluid Mech.* **506**, 45–78.
SHIH, W.C.L., WANG, C., COLES, D. & ROSHKO, A. 1993 Experiments on flow past rough circular cylinders at large Reynolds numbers. *J. Wind Engn Ind. Aerodyn.* **49** (1–3), 351–368.
SOUMYA, S. & PRAKASH, K.A. 2017 Effect of splitter plate on passive control and drag reduction for fluid flow past an elliptic cylinder. *Ocean Engn* **141**, 351–374.
STRYKOWSKI, P.J. & SREENIVASAN, K.R. 1990 On the formation and suppression of vortex 'shedding' at low Reynolds numbers. *J. Fluid Mech.* **218**, 71–107.
SUN, Y., WANG, J., FAN, D., ZHENG, H. & HU, Z. 2022 The roles of rigid splitter plates in flow-induced vibration of a circular cylinder. *Phys. Fluids* **34** (11), 114114.
THOMPSON, M.C., LEWEKE, T. & PROVANSAL, M. 2001 Kinematics and dynamics of sphere wake transition. *J. Fluid. Struct.* **15** (3–4), 575–585.
TOKUMARU, P.T. & DIMOTAKIS, P.E. 1991 Rotary oscillatory control of a cylinder wake. *J. Fluid Mech.* **224**, 77–90.
VU, H.C., AHN, J. & HWANG, J.H. 2016 Numerical investigation of flow around circular cylinder with splitter plate. *KSCE J. Civil Engn* **20** (6), 2559–2568.
WANG, J.J., ZHANG, P.F. & WU, K. 2006 Drag reduction of a circular cylinder using an upstream rod. *Flow Turbul. Combust.* **76** (1), 83–101.
WANG, R., BAO, Y., ZHOU, D., ZHU, H., PING, H., HAN, Z., SERSON, D. & XU, H. 2019 Flow instabilities in the wake of a circular cylinder with parallel dual splitter plates attached. *J. Fluid Mech.* **874**, 299–338.
WILLIAMSON, C.H.K. 1996 Vortex dynamics in the cylinder wake. *Annu. Rev. Fluid Mech.* **28** (1), 477–539.
WILLIAMSON, C.H.K. & ROSHKO, A. 1988 Vortex formation in the wake of an oscillating cylinder. *J. Fluid. Struct.* **2** (4), 355–381.
XU, S.J., ZHOU, Y. & WANG, M.H. 2006 A symmetric binary-vortex street behind a longitudinally oscillating cylinder. *J. Fluid Mech.* **556**, 27–43.
YOON, D., YANG, K. & CHOI, C. 2012 Three-dimensional wake structures and aerodynamic coefficients for flow past an inclined square cylinder. *J. Wind Engng Ind. Aerodyn.* **101**, 34–42.

YOU, D., CHOI, H., CHOI, M.R. & KANG, S.H. 1998 Control of flow-induced noise behind a circular cylinder using splitter plates. *AIAA J.* **3611**, 1961–1967.

ZDRAVKOVICH, M.M. 1997 *Flow around circular cylinders, Volume 1: Fundamentals*. Oxford University Press.

ZHU, H. & LIU, W. 2020 Flow control and vibration response of a circular cylinder attached with a wavy plate. *Ocean Engn* **212**, 107537.